

PHOTOACOUSTIC MICROSCOPY OF MALIGNANT MELANOMA IN THE
IN VIVO MOUSE MODEL

BY

Jacob W. STALEY

Submitted to the graduate degree program in Bioengineering and the Graduate
Faculty of the University of Kansas in partial fulfillment of the requirements for
the degree of Master of Science.

Chairperson

Committee members

Date Defended: _____

The Thesis Committee for Jacob W. STALEY
certifies that this is the approved version of the following thesis:

PHOTOACOUSTIC MICROSCOPY OF MALIGNANT MELANOMA IN THE
IN VIVO MOUSE MODEL

Chairperson

Date approved: _____

ABSTRACT

PHOTOACOUSTIC MICROSCOPY OF MALIGNANT MELANOMA IN THE *IN VIVO* MOUSE MODEL. (2010)

Jacob W. Staley, B.Sc., University of Kansas

Chair of Advisory Committee: Dr. Xinmai Yang

Current imaging modalities such as magnetic resonance imaging (MRI), computed tomography (CT), optical coherent tomography (OCT), and ultrasound have various drawbacks when applied to imaging malignant tumors and associated angiogenesis. These drawbacks range from the need to use toxic contrast agents to a lack of penetration depth and sufficient contrast. Photoacoustic microscopy improves on these techniques by utilizing optical absorption of biological components and acquiring acoustic waves from optical stimulation, yielding high contrast, while retaining high resolution and sufficient depth penetration.

To address the limitations of current imaging modalities, researchers are investigating the application of photoacoustic microscopy in the early detection of malignant tumors. This thesis presents the results of applying noninvasive photoacoustic microscopy to detect and track the progression of subcutaneous melanoma tumors and melanoma tumor growth in the brain of live mice *in vivo*, as well as demonstrating the use of NIR-dye as a contrast agent for future use with photoacoustic tumor imaging.

*for those that have provided shoulders to stand on, and to those who provided shoulders on
which to lean*

ACKNOWLEDGEMENTS

First and foremost, I would like to thank my advisor, Dr. Xinmai Yang, for giving me the opportunity to work under him and providing support throughout my time in his lab. His constant ideas and drive were instrumental in my completion of this body of work.

I would also like to thank Dr. Carl Luchies for his guidance and invaluable advice during my time in KU's Bioengineering program and research work. Also, his willingness to serve on my committee despite his enormous responsibilities was a testament to his dedication to the student body.

I must thank Dr. Laird Forrest for his help with all things melanoma, his willingness to participate in avenues of interdisciplinary research, and for serving on my committee. I would also like to acknowledge Taryn Bagby from Dr. Forrest's lab, as she was a key player in the success of the subcutaneous melanoma growth.

Finally, I would like to thank Mark Cohen, MD, and Patrick Grogen from the University of Kansas Medical Center. Without their help the brain tumor portion of this thesis, as well as our paper, would not exist.

TABLE OF CONTENTS

ABSTRACT	iii
ACKNOWLEDGEMENTS	v
TABLE OF CONTENTS	vi
LIST OF FIGURES	viii
1 Cancer	1
1.1 Research Objectives	1
1.2 Melanoma	1
1.3 Anatomy of Tumors	4
1.4 Current and Competing Imaging Modalities	9
2 Photoacoustics	13
2.1 Introduction	13
2.2 History	14
2.3 Photoacoustic Theory	14
2.4 Light Behavior In Biological Tissue	18
2.5 Photoacoustic Microscopy (PAM)	22
2.6 Photoacoustic Applications	27
3 PAM System	32
3.1 Control System	32
3.2 Dark-field PAM	34
4 Subcutaneous malignant melanoma in the <i>in vivo</i> mouse model	36
4.1 Introduction	36
4.2 Materials and Methods	37
4.3 Results and Discussion	39

4.4	Conclusions	42
5	Photoacoustic Discrimination of Malignant Melanoma	
	Using NIR-dye as Contrast Agent	43
5.1	Introduction	43
5.2	Materials and Methods	45
5.3	Results and Discussion	46
5.4	Conclusions	49
6	Noninvasive Photoacoustic Microscopy of Brain Tumors in Live Mice	
	<i>* Chapter has been submitted to the Journal of Biomedical Optics</i>	50
6.1	Introduction	50
6.2	Materials and Methods	52
6.3	Results and Discussion	56
6.4	Conclusions	63

LIST OF FIGURES

1.1	Anatomical diagram of the epidermis, dermis, and subcutaneous layers of skin.	6
1.2	Superficial nodular melanoma	7
2.1	Dominating chromophores in biological tissue	21
2.2	Incident pulsed laser light inducing thermoelastic expansion	23
2.3	Photoacoustic dark-field illumination	24
3.1	State-machine of the control system	33
3.2	PAM system hardware diagram	35
4.1	Anatomy of melanoma growth after subcutaneous cell delivery . . .	38
4.2	Anatomical and PA images of subcutaneous melanoma	40
4.3	PA images of a metastatic melanoma on the spine	42
5.1	NIR-dye depot and melanoma tumor	46
5.2	PA images comparing dye and tumor - 764nm and 988 nm wavelengths	47
5.3	Normalized intensity plots of B-scans - 764 nm and 988 nm	48
6.1	Brain inoculation site	54
6.2	PAM images of brain tumor in mouse <i>A</i>	57
6.3	Maximum amplitude projection in 3D space	59
6.4	B-scan of brain tumor in mouse <i>A</i>	60
6.5	Brain tumor progression in mouse <i>B</i>	62

1 Cancer

1.1 Research Objectives

Photoacoustic Microscopy is an emerging biomedical imaging technique in the field of cancer detection and imaging ¹. Progress over the last twenty years in the advancement of laser technology and optoacoustic detection have given researchers the tools to obtain accurate and informative data. Utilizing the currently available progress in the area of photoacoustics, the discovery and analysis of metastatic melanoma growth, and the accompanying attributes in biological tissue, is sought. Photoacoustic detection, imaging, and differentiation in early stages of growth of malignant melanoma is the focus of this research.

1.2 Melanoma

Cancer of the skin is the most common form of cancers and annually accounts for nearly half of all reported cancer cases. One form of skin cancer, cutaneous melanoma, is considered to be the most widely metastasizing neoplastic disease while having one of the least predictable patterns of spread ². Since melanoma currently has no curative treatment once the tumor has metastasized, there is con-

siderable clinical interest in the discovery, diagnosis, and treatment of melanoma in its earliest stages. More than 108,000 new cases of melanoma were diagnosed in 2007 according to the American Academy of Dermatology. Despite an overall decline in cancer rates during the time period between 1995 and 2004, diagnosis of melanoma has increased by more than 1% per year during the same time span. In fact this trend in diagnosis increase has been seen in the last thirty years. Melanoma incidence increased from 7 cases per 100,000 in 1973 to greater than 18 cases per 100,000 in 2003. One staggering statistic of melanoma is the disease can be attributed to causing 75% of skin cancer deaths just within the United States³. As a result of melanomas ability to aggressively metastasize and proliferate, the American Cancer Society estimated that 8,420 people would die of malignant melanoma in 2008 alone.

Similar to many other forms of cancer, melanoma effects a wide range of age groups. Rates are seen to increase with age, however, and reach their peak in adults in their 80's, but it is not uncommon for those under 30 to be diagnosed with the disease. Although melanoma has been found to afflict Caucasian males in greatest numbers, it is not limited to that specific demographic and can be found across all genders and ethnicities.

As with all types of metastasizing cancers, melanoma has the ability to invade and proliferate throughout the body in various soft and hard tissues. In its later stages, where vertical growth is prevalent, melanoma often invades the dermis

and subcutaneous layers of skin, gaining access to vital transportation networks through the lymphatic system and rich network of blood vessels. Metastasis are found in 15 to 40% of all patients diagnosed with systemic malignancies, the third most common being melanoma (10-20%). One aspect that makes melanoma so deadly is the fact that it has the highest propensity to metastasize to the brain and carcinomas tend to be multiple⁴.

Gabriella et al. found that patients diagnosed with cutaneous malignant melanoma have an approximate chance of 25-35% of developing recurrent disease. Recurrence has many factors involved including primary tumor thickness, and ulceration of the primary tumor⁵. Once recurrence of malignant melanoma has occurred attributes of the primary tumor provide little to no correlating information on patient survival, however region and tissue recurrence play an important role in predicting survival rates among patients. The group also found an overall patient survival rate of 25% at 5 years after the first recurrence and 18% by 10 years. Looking specifically at regional recurrence in the same population, if the site of recurrence was local to the original site the survival rate was found to be 82%, compared with 30% among those with lymph node, or a primary regional in-transit recurrence. When looking at distant site or locoregional recurrences, patient survival rates rarely lasted longer than 3 years⁶. Beyond location, survival rate is heavily influenced by types of metastases. Patients with CNS, bone, liver, or visceral distant metastases had significantly lower ($p < 0.0001$) survival rates than

those with distant skin, pulmonary, or lymph node metastases ⁵.

1.3 Anatomy of Tumors

Subcutaneous

Skin is composed of three main layers - the epidermis, dermis, and subcutaneous layer. The epidermis is the thin outermost layer, which itself is made up of five sub-layers:

- stratum basale
- stratum spinosum
- stratum granulosum
- stratum lcidum
- stratum corneum

Residing below the epidermis is the dermis. The dermis, in a non-layered fashion, is primarily composed of three types of tissue:

- elastic tissue
- reticular fibers
- collagen

The dermis contains many specialized cells and structures including hair follicles, sebaceous (oil), apocrine (scent), and eccrine (sweat) glands. The dermis layer is also rich in blood vessels and nerves which transmit sensations of temperature, pressure, and pain. The final layer is the subcutaneous layer, which is primarily made up of fat and connective tissue, and helps regulate temperature of the body and the skin itself. It is here that large blood vessels and nerves exist, protected by the two more superficial layers of the skin - the epidermis and dermis.

Melanoma is a malignancy that arises from melanocytes, which are the pigment producing cells that reside in the lower portion of the epidermis, as seen in Fig. 1.1. Melanocytes, through the production of melanin via melanogenesis, are responsible for giving skin its characteristic color and protecting the body from ultraviolet radiation ⁷. Melanocytes are also found in the eyes, ears, GI tract, and oral and genital mucous membranes.

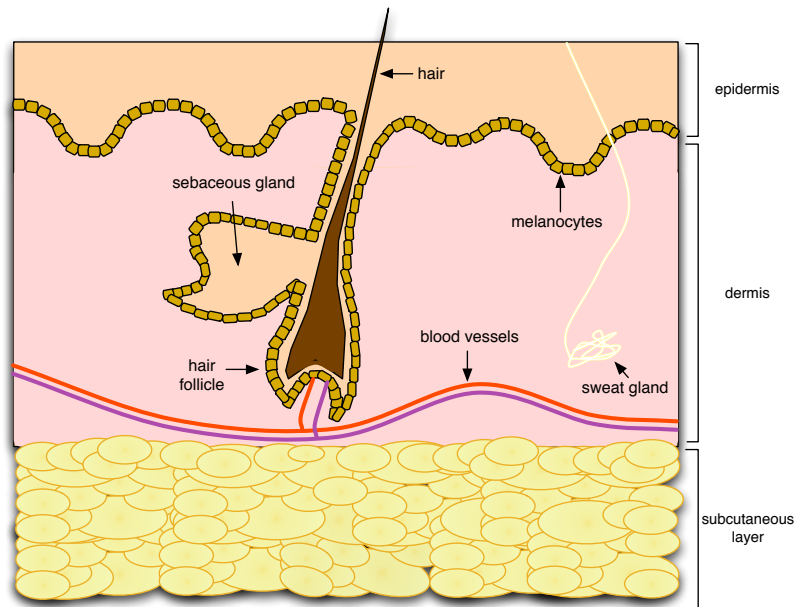


Figure 1.1: Anatomical diagram of the epidermis, dermis, and subcutaneous layers of skin.

Typically radial tumor growth occurs in the epidermis layer and is followed by a vertical growth phase, which infiltrates the underlying dermis and often subcutaneous layer if progression is uninhibited⁸⁻¹⁰. A typical nodular melanoma tumor that permeates the epidermis and dermis layer can be seen in Fig. 1.2.

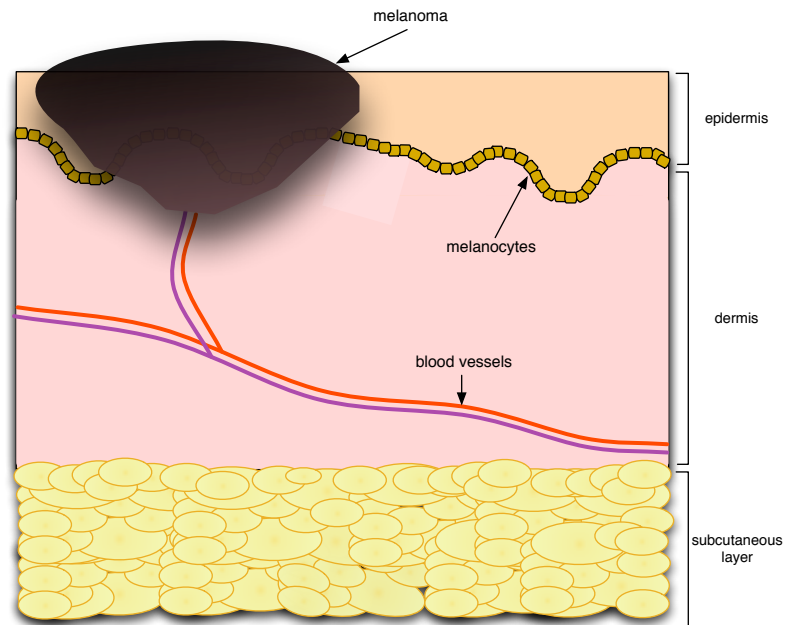


Figure 1.2: Typical superficial nodular melanoma arising from malignant growth of melanocytes in the epidermis.

Brain

There has been a great deal of work on explanation of brain metastasis and metastasis in general. Currently there seems to be two theories that typically are used separately or in conjunction with one another. The first proposed by *Paget*, describes a nonrandom pattern of metastasis that uses a theory of 'seed' and 'soil'. More specifically, *Paget* postured that specific tumor cells had an affinity for certain organs, thus requiring that tumor cells (seeds) metastasize and form distant tumors when in contact with a compatible organ (soil). There has been work that shows certain tumors metastasize to specific organs independent of

influential factors such as blood flow, tumor cell count, and vascular anatomy, which supports this theory¹¹. The more mechanical hypothesis was put forth by *Ewing*, in which he stated metastatic proliferation is a consequence of vascular and anatomical structure. This removes the requirement of 'seed' and 'soil' and is more concerned with anatomical factors such as lymphatic drainage or efferent venous circulation¹².

In order for metastatic growth to occur and makes its way to the brain, numerous conditions have to be met. The first being the proper network of vasculature to support the tumor mass, which arises from the secretion of proangiogenic factors by host and tumor cells alike, and the absence of antiangiogenic factors. Proceeding this there must occur an expression of a series of enzymes that allow invasion of local host vascular or lymphatic channels. If these conditions are met tumorous cells are able to grow into these channels and distribute tumor emboli into the circulatory system. If the emboli survive immune defenses and other innate obstacles and reach receptive organs, the process continues, resulting in metastasis of metastases, and consequently forming the metastatic cascade¹¹. It is through this process that it is believed metastatic tumors form within the brain.

1.4 Current and Competing Imaging Modalities

Magnetic Resonance Imaging (MRI)

MRI is a well established technique in the field of biomedical imaging. Given its high contrast capabilities it is often used within radiology to visualize the internal structure of the body. Various research has been conducted in the area of skin tumors using MRI as an imaging technique. *Kim et al.* showed MRI can be used to image manifestations of skin tumors ranging from discrete mass lesions of the dermis and epidermis to subcutis mass lesions¹³. *Thies et al.* demonstrated the feasibility of MRI in detecting melanoma metastases in a xenograft scid mouse model. Using T2 weighed images, primary melanoma lesions appeared hyper-intense and were clearly discernible from surrounding tissue. MR analyses forty days post excision of the primary tumor nodules revealed hyper-intense T2 weighed images of suspect melanoma lesions in various distant organs¹⁴.

Although MRI provides many appealing attributes and has shown successful applications, there are certain potential drawbacks to using this modality. First is the cost associated with undergoing MRI scans. It is typically one of the most expensive biomedical imaging techniques to acquire with regards to hardware costs and similarly expensive for the patients to use. Beyond associated monetary expenses there is another more serious drawback to the technology. MRI has

been shown to be unable to reliably discriminate benign from malignant tumors¹⁵. Another limiting factor arises from the inclusion of stipulations with respect to the patient. Patients with pre-existing kidney conditions are strongly discouraged from using gadolinium contrast agents, which are intravenously delivered to enhance MRI films, due to an FDA black box warning which states a possible complication from the contrast agent can cause nephrogenic systemic fibrosis. Also, patients with implants containing ferrous materials or electronics may prove unable to undergo MRI scanning due to the possible complications that can arise from the associated magnetic field.

Optical Coherent Tomography (OCT)

OCT was originally presented to the medical community as a way to noninvasively examine the human eye. However, the technology was eventually adopted to use with human skin studies. OCT operates by scanning a low-coherence light source across tissue and uses principles based on interferometry to image regions of interest. Specifically, an optical source irradiates tissue and the back-scattered light is measured by correlating it with light that has traveled a known reference path. OCT has a high degree of resolution, comparable to low power microscopes (better than 10 μm), but suffers from lack of penetration depth. OCT's imaging depth is limited to 1-2 mm depth due to the lack of backscattered light collected from the medium, which results from absorption and/or high degree

of forward-scattering of light. This is a severe drawback to open use of OCT in many applications of interest. Due to the lack of penetration depth OCT is typically limited to the most superficial of applications with respect to imaging highly turbid and absorbing media such as skin and melanoma.

Ultrasound

Researchers and medical doctors alike have utilized ultrasound imaging techniques to confirm and substantiate suspect tumor growth. Melanocytic lesions have been examined using ultrasound (20-MHz) and high-frequency ultrasound (50- to 100-MHz)¹⁵. Tumors typically show up as echoluscent areas on ultrasound images, which are often difficult to discern from surrounding soft tissue. Although ultrasound provides excellent axial and lateral resolution, it suffers from lack of contrast. This lack of contrast prevents purely ultrasound imaging techniques from use in the diagnosis of melanoma currently.

Photoacoustic Imaging

Looking at the other imaging modalities it is apparent they all have their various drawbacks. The range of limitations is wide across the spectrum of technologies. Most suffer from either lack of sufficient contrast, the ability to accurately discriminate between cancerous and non-cancerous tissue, penetration depth, or a combination of all the above. The lack of quantifiable hemodynamic data is also

another downfall in these modalities in the realm of cancerous tissue imaging and diagnostics.

Compared to competing technologies, photoacoustic imaging (PAI) combines a great deal of advantages over the others while minimizing disadvantages, making it an excellent modality in the application of targeted tissue imaging and diagnostics. PAM operates by depositing laser energy into an absorbing medium and recording the produced acoustic signal. PAM has been shown to produce micron-scale resolution in superficial applications^{16–18} as well as achieving success in deep tissue imaging^{19–21}. PAM is able to overcome a great portion of the drawbacks of the aforementioned modalities due to the fusion of optical and ultrasound techniques. More specifically, the photons in the optical portion are used as the energy source, but the information is gathered from the resultant ultrasound signal. This allows for greater preservation of information and eliminates the scattering and absorption limits typically found in purely optical imaging techniques. To further illustrate this an in depth discussion about photoacoustic theory will be discussed in Chapter 2.

2 Photoacoustics

2.1 Introduction

The benefits of photoacoustic imaging in various areas of medicine are many and primarily result from the high contrast properties of optical light and high resolution found in ultrasonic imaging. The highly absorptive properties of biological tissue with respect to visible and near-infrared (NIR) electromagnetic spectrum allow for discovery of functional parameters in various tissues^{22,23,17,24–32}, hemodynamics monitoring^{23,17,24,25,28,30,31}, and imaging of tissue abnormalities^{33,32,34,30}. Within these realms photoacoustic imaging is a blossoming field that shows great promise. Beyond the superior contrast and resolution that PAM offers, it also allows for greater depth penetration compared to other purely optical techniques due to the lack of attenuation and scattering of the acoustic signal when compared to a purely optical source.

This chapter will serve as an introduction to the technical aspects of PAM. It will start with a brief history, progress into the physics behind photoacoustics, discuss the underlying principles of the PAM system, and end with various applications of the technique in numerous realms of research.

2.2 History

The technique is based on the optoacoustic effect, which was first discovered by Alexander Graham Bell in 1880. Bell noted that when a thin sheet of rubber was struck by modulated light a perceptible sound was generated³⁵. This phenomenon was later discovered to exist in other materials including liquid, gaseous, and biological tissue. As laser technology advanced, the field of photoacoustic spectroscopy emerged, which is concerned with the excitation of gaseous media in order to yield detectable sound³⁶. As the field progressed, work in areas of photoacoustic microscopy and tomography developed, which focuses on the study of the optoacoustic effect applied to biological tissue. The optoacoustic effect can be found in any medium that absorbs a variable electromagnetic flux. Both optoacoustics and photoacoustics relate the same interaction of absorption of electromagnetic radiation and the production of acoustic waves, with the former encompassing the more general case of excitation of sound as a result of deposition of electromagnetic energy, the later more specifically deals with short pulsed laser light as the excitation source (i.e. electromagnetic energy)³⁶.

2.3 Photoacoustic Theory

Using a collimated pulsed laser beam to irradiate biological tissue creates a rapid and localized temperature rise, which promptly induces thermal expansion, thus

producing a sudden increase in pressure. Due to the pulsed nature of the incident light and brief rapid heating of the tissue we can assume two necessary conditions are met to produce photoacoustic waves - thermal and stress confinement²⁴. Thermal confinement is possible when the energy deposition occurs quicker than the time needed for thermal relaxation. Thermal relaxation time gives an approximation to the time an absorber (i.e. heated volume) requires in order to cool to ambient temperature³⁷. In the case of photoacoustics this is governed by the beam width duration, τ_L , which is on the nanosecond scale. Since τ_L is much shorter than heat diffusion time, τ_{th} , given by

$$\tau_L < \tau_{th} = \frac{d_p^2}{4\kappa} \quad (2.1)$$

where d_p represents the characteristic length (i.e. light penetration depth), and κ (cm^2/s) is the thermal conductivity of the the medium ($\sim 0.14 \text{ mm}^2 \text{ s}^{-1}$ in tissue³⁸), we can conclude instantaneous heating of the medium since thermal diffusion can be ignored³⁹.

The second condition, stress confinement, describes the time for the stress generated due to thermoelastic expansion to exceed the location of the heated region. More specifically, a short laser pulse ensures cessation of said pulse before generation of the acoustic wave. This prevents diffusion of heat to surrounding

tissue and eliminates consequences such as reduced conversion efficiency of absorbed energy to heat. Stress time, τ_s (s), is established by

$$\tau_L < \tau_s = \frac{d_p}{c_s} \quad (2.2)$$

where c_s is the speed of sound in the medium. Assuming these defined quantities are satisfied we can investigate pressure distributions and wave generation.

Generally the strength of the illumination source is proportional to the amount of heat generated by tissue. Absorbed light is converted into heat through various mechanisms and is related by the general heating function. The heating function describes the amount of thermal energy converted at a location \mathbf{r} and time t by incident electromagnetic radiation per unit volume per unit time, shown by

$$H(\mathbf{r}, t) = A(\mathbf{r})\delta(t) \quad (2.3)$$

where $A(\mathbf{r})$ is the heat deposited per unit volume. It should be noted that the heating function assumes instantaneous heating, which is established by equation (2.1).

There is a resultant expansion of the absorber in response to the temperature rise from energy absorption. The change in volume produces an increase in pressure (kg/ms²) given by

$$p_i(\mathbf{r}) = \frac{\beta c_s^2}{C_p} A(\mathbf{r}) = \Gamma A(\mathbf{r}) \quad (2.4)$$

where β is the volume thermal expansivity, C_p is the constant pressure specific heat capacity, and Γ is the dimensionless Grüneisen coefficient, which relates the conversion efficiency of thermal energy to stress. Values of Γ typically range from 0.11 to 0.125 in biological tissue⁴⁰. Given equations (2.3) and (2.4) we can describe the time dependent electromagnetic absorption and pressure wave at a position \mathbf{r} and time t in an acoustically homogenous medium with fluid like properties by the following wave equation⁴¹

$$\nabla^2 p(\mathbf{r}, t) - \frac{1}{c_s^2} \frac{\partial^2}{\partial t^2} p(\mathbf{r}, t) = -\frac{\beta}{C_p} \frac{\partial}{\partial t} H(\mathbf{r}, t) \quad (2.5)$$

The pressure wave that is generated radiates in all directions, which allows the acoustic energy to be split evenly between the initial reflected pressure distribution and the initial transmitted pressure distribution. It should be noted that the initial transmitted pressure distribution propagates away from the source of laser irradiation.

tion. The speed at which acoustic waves propagate in a medium is determined by the intrinsic properties of the medium of interest. Since most biological tissue is highly comprised of water, the value given to the speed of acoustic propagation is $\sim 1.5 \text{ mm}/\mu\text{s}$, which is the speed of sound in water.

2.4 Light Behavior In Biological Tissue

Light propagation in tissue has many attributes that are of concern for photoacoustics. Typically optical interaction between tissue and light is characterized by scattering, thus tissue is often referred to as scattering media or turbid media. In general scattering is governed by two main ideas: single and multiple scattering theories. In single scattering theory, randomly distributed scattering objects reside at a mean distance from one another much greater than the period of the wavelength and the scatterer size. A medium with these attributes can be considered loosely packed with scatterers, and due to the distance and size, scattering events are considered independent. If sizing and space constraints are not met, the medium is thought of as being densely packed, and single scattering theory is not valid. In order to quantify the amount of scattering that is innate to a given medium, μ_s (scattering coefficient) is used and defined as the scattering probability of a photon per unit length the photon travels within the medium.

Absorption is found to be relatively weak in the 400-1350 nm spectral region, producing a mean absorption length, i.e. the mean distance traveled before an

absorption event occurs, of roughly 10-100 mm. When describing absorption, μ_a (absorption coefficient) is used to define the probability of photon absorption per unit length within a medium. The reciprocal of μ_a , the mean absorption length, is the distance through the medium in which the intensity of the incident light source falls by e^{-1} . Absorption of a photon gives rise to excitation of an electron from a molecule from a ground state to an excited state. Multiple possible outcomes can occur depending on the transition of the electron back to a ground state. The excited electron can luminesce, i.e. give off another photon, or generate heat, which is the property of interest in photoacoustics. The overall effect of absorption on the propagating light is a reduction of the intensity as it makes its way through the medium and can be described by

$$\frac{dI}{I} = -\mu_a dl \quad (2.6)$$

where I relates the light intensity and l denotes the distance of light propagation. The equation describes how the medium absorbs the same fractional value dI/I of incident intensity for each consecutive layer dl for a constant absorption coefficient, μ_a (typically mm^{-1}). Integrating both sides of this equation leads to the Beer-Lambert law

$$I = I_0 e^{-\mu_a l} \quad (2.7)$$

where I_0 is the incident intensity, i.e. when $l = 0$. The law gives a relation of the exponential decay of the intensity of light as it is reduced due to absorption as the light travels through the medium along the distance l . There are limitations to the Beer-Lambert law however which arise due to assumptions made based upon the light source and medium. The assumptions typically cause experimental results, when compared to expected values, to deviate⁴². For instance, the law assumes impinging light on the medium is perfectly collimated and monochromatic in nature. Further restrictions are placed on the medium as well, demanding that the medium must be purely and uniformly absorbing.

Tissue chromophores are responsible for giving a molecule its color due to the absorption of wavelengths in the NIR, with each particular chromophore having its own unique spectrum. The total absorption in biological tissue is the sum of the contributions gained from each respective chromophore²⁴. Therefore, total light absorption at a specific wavelength is dependent on the concentration and type of chromophore within the absorbing tissue. Optical absorption of light in biological tissue arises primarily from the dominating chromophores of hemoglobin, melanin, and water. In the ultraviolet (UV) region hemoglobin, as well as melanin,

strongly absorb light. As the wavelength increases the trend of absorption by both chromophores is reduced as seen in Fig. 2.1 (Wang, 2007)²².

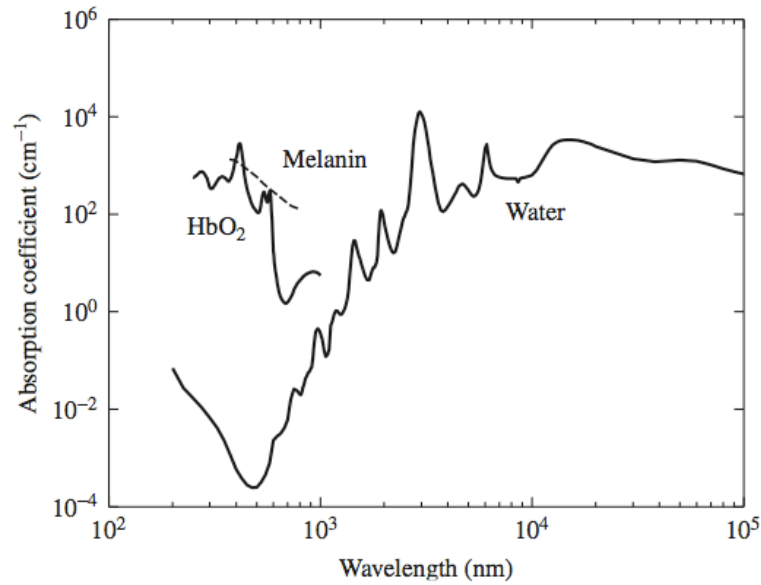


Figure 2.1: Dominating chromophores in biological tissue (Wang, 2007)²²

Fig. 2.1 shows that in the UV and NIR spectrum water has minimal absorption, which provides a 'window' of tissue transparency, allowing light propagation in the NIR region to travel through several centimeters of tissue. However, as wavelength increases there is a large increase in the absorption coefficient with respect to water and a severe reduction in propagation depth of light.

By combining μ_s with μ_a it is possible to describe the total interaction between light and tissue and is given by

$$\mu_t = \mu_s + \mu_a \quad (2.8)$$

where μ_t is the total attenuation coefficient, which is also referred to as the extinction coefficient²². The inverse of the total attenuation coefficient, μ_t^{-1} , is referred to as the mean free path, and represents the distance traveled by a photon between interactions. Given these new definitions it is possible to describe a relationship, exponentially, between the collimated beam intensity I and the incident intensity I_0 that is transmitted through a medium of length l . Under the stipulation that single scattering occurs this is represented by

$$I = I_0 e^{-\mu_t l} \quad (2.9)$$

2.5 Photoacoustic Microscopy (PAM)

PAM is a hybrid imaging modality which utilizes the intersection of optical and acoustical properties. In this application the photoacoustic effect is achieved by irradiating tissue, through dark-field illumination, with non-ionizing laser pulses which are absorbed by tissue and consequently induce transient thermoelastic expansion as seen in Fig. 2.2.

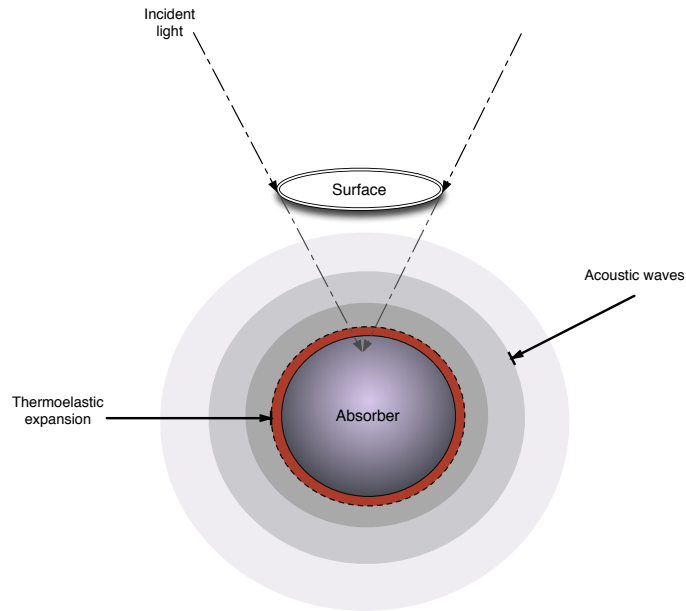


Figure 2.2: Incident pulsed laser light is delivered to an absorber of interest using dark-field illumination creating acoustic waves that radiate from the absorber.

The thermoelastic expansion produces ultrasonic waves and these propagating acoustic waves are captured via acoustic transducers, which are digitized into a voltage signal quantifiable by a digital acquisition card or an oscilloscope. If the transducer is placed on the opposite side of the incident laser irradiation, it is considered a transmission mode measurement. If the transducer collects acoustic waves on the same side as the laser irradiation, the measurement is a reflection mode measurement. An example of a reflection mode setup is shown in Fig. 2.3.

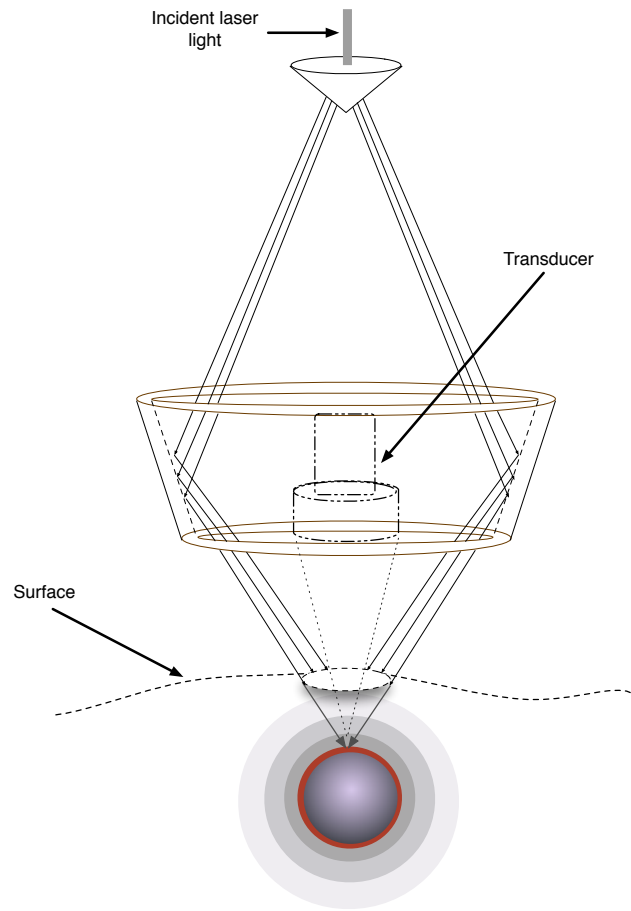


Figure 2.3: Photoacoustic setup for capturing reflected acoustic waves using dark-field illumination.

The advantages of using light as an energy source to produce the acoustic signal are many. Acoustic signals are much more robust in biological tissue and are typically scattered 2-3 times less than optical signals³², thus allowing an increase in penetration depth while maintaining spatial resolution.

One important aspect to note is that the initial reflected and transmitted pressure distributions both contribute to the acquired signal when using either method - transmission or reflection mode. This phenomenon arises from a combination

of acoustic mismatches that typically occur at boundaries of absorbing mediums. These differing acoustic impedances create a free boundary, which causes acoustic energy to be reflected back into the medium, but with a negative amplitude. Also of interest is the fact that different diameter absorbers will produce waves of differing frequency when encountering the same incident light pulse. Looking at the heating function from equation (2.3) we see it is spatially and temporally modulated. Photoacoustic waves are in turn modulated by the heating function, thus small diameter absorbers produce different spatial profiles for the same temporal profile as a large diameter absorber. This produces an important result, which is as the diameter of the absorber increases the frequency of the generated photoacoustic wave decreases. Conversely, as the diameter of the absorber decreases there is an increase in the frequency of the photoacoustic wave. This fundamental response to absorber diameter plays an important role in photoacoustics, requiring the use of wide-band transducers in order to detect the spectrum of acoustic waves generated from biological tissue³⁹.

The analysis of photoacoustic signals encompasses many aspects, but is primarily concerned with determination of the absorber's characteristic optical properties. The optical properties of interest are commonly the refractive index, n , scattering coefficient, μ_s , absorption coefficient, μ_a , and anisotropy factor, g . These properties play an important role in identification of various tissue types, as well as the pathologies that manifest within them. More specifically, it is possible to identify

various forms of tissues and pathologies simply by matching the above properties with known experimental values.

By utilizing the speed of sound approximation in biological tissue it is possible to determine the depth from the absorber to the transducer. Using the approximation of sound in tissue, conversion from the pressure *vs* time signal to a pressure *vs* distance signal is a simple and straightforward process. Typically the maximum of the waveform is taken to be the distance from the absorber surface to the transducer.

The photoacoustic data recorded by the computer is used to reconstruct images in the form of an A-scan, B-scan, 2-D, or 3-D image. A-scans serve as a way to visualize the waveform generated depth-wise into the tissue for a single point of interest. This allows analysis of the resultant thermoelastic response to a single excitation point (e.g. one firing of the laser), which reveals how well the medium of interest absorbs optical energy and just as importantly the depth at which this occurs. B-scans consist of a frame (i.e. a single raster line scan) of A-scans, which allows for what is essentially a slice along the *z*-axis (depth) to be visualized. Producing 2-D images is a straightforward process of simply taking the maximum amplitude projection (MAP) of each A-scan and forming a series of MAP B-scans that are pieced together in order to form the complete image from a top-down view. Constructing 3-D images is similarly simple, only requiring slight manipulation of the recorded data into a 3-D matrix form that existing software (e.g. Volview) can

use to construct the 3-dimensional structure.

2.6 Photoacoustic Applications

Oncology Applications

The innate and highly varying optical absorption coefficients of biological tissue provide an environment for photoacoustic imaging to excel. Due to the aforementioned variations, photoacoustics provides a well suited imaging technique for visualizing the distinction between malignant and healthy tissue, as well as surrounding vasculature.

Copland et al. utilized photoacoustic techniques in conjunction with conjugated gold nanoparticles (NPs) to demonstrate the ability to image breast cancer cells deep within tissue. By conjugating commercially available spherical gold NPs to a monoclonal antibody (Herceptin®) it was shown that an imaging depth of 6.5 cm could be reached when targeting a tumor as small as 0.25 cm. Along with deep penetration, high resolution was also obtained, yielding 0.5 mm in the *in vitro* experiments⁴³. This work exemplified the abilities of photoacoustics in the area of targeted tumor detection deep within areas of interest such as breast tissue.

Zhang et al. utilized photoacoustic microscopy to image subcutaneously inoc-

ulated B16 melanoma in a immunocompromised nude mouse. Complimentary images were produced revealing surrounding vasculature as well as the melanoma tumor by varying the optical wavelength to match the absorption coefficients of interest. The average ratio of vasculature to background in PA amplitude was 13 ± 0.89 at 584 nm wavelength. When using 764 nm wavelength the average ratio of the melanoma tumor to the surrounding vasculature was 29 ± 3 , and when compared to the background was as large as 68 ± 5 . Using these techniques they were able to successfully show the depth profile of the tumorous region as well, which is important in diagnosis and forming a therapy strategy¹⁷.

Oh et al. produced results that showed 3-D structures of subcutaneous melanoma as well as surrounding vasculature. The system used was comprised of a pair of pulsed lasers that enabled two wavelengths to be used, one based on the absorption coefficient of blood (584 nm) and the other targeted towards melanoma (764 nm). There were some drawbacks to the system however. For instance, the time to image an 8 X 8-mm area took approximately 65 min and doubled when using both wavelengths. Also, due to the high central frequency of the transducer used (50 MHz), the imaging depth was sacrificed as well as the accuracy of the depth profile of the tumor itself³³.

Targeted applications and contrast agents have also shown great promise in this area with respect to photoacoustics. *Mallidi et al.* conjugated gold nanoparticles to antibodies in order to target epidermal growth factor receptors. Gold nanoparticles

undergo molecular specific aggregation after binding to cell surface receptors, which causes a red shift in their plasmon resonance frequency⁴⁴. In order to utilize this effect they implanted subcutaneous tumor-mimicking gelatin implants in *ex vivo* mouse tissue and photoacoustically imaged the samples. Their results suggest that with the use of targeted gold nanoparticles it is possible to detect, and further be highly selective, of cancer cells using multiwavelength photoacoustic imaging.

Vascular and hemodynamic applications

A great deal of research has been conducted in the area of microvasculature imaging and hemodynamics observation with photoacoustics. PAM, given its exceptional contrast abilities due to the absorption properties found in blood vessels, is ideal for these applications.

Laufer et al. used pulsed photoacoustic spectroscopy to quantify chromosphere concentrations noninvasively using tissue phantoms with embedded polymethylmethacrylate tubes carrying saline suspended red blood cells. Using an optical parametric oscillator to generate wavelengths of 740-1040 nm, they were able to quantify hemodynamic properties by extracting the signal amplitude and effective attenuation coefficient from the photoacoustic signals. From these results forward models based on diffusion theory were used to decipher relative concentrations of HbO₂ and Hb, as well as blood oxygen saturation (SO₂) and total hemoglobin concentrations. The photoacoustically discovered values of oxygen saturation were

found to have an accuracy of $\pm 4\%$ SO_2 from signal amplitude values and $\pm 2.5\%$ SO_2 for effective attenuation spectra with a oxygen saturation sensitivity of $\pm 1\%$ SO_2 using the technique⁴⁵.

Xiang et al. used a Sprague Dawley rat as a carrier for the gliosarcoma cell line in order to photoacoustically visualize neovascularization in tumor angiogenesis⁴⁶. The cells were subcutaneously injected into the back of the rat and photoacoustic images were obtained over the incubation period of 5, 8, 11, 14 days. A photoacoustic system using a single-element ultrasonic transducer was scanned over 2π angular area using step sizes of 1.8° . This resulted in an approximate scanning time of 15 minutes that produced images that clearly revealed the proliferation of surrounding vasculature and the subsequent neovascularization associated with the increased angiogenesis caused by tumor growth.

Research conducted by *Li* et al. demonstrated the ability to measure hemoglobin oxygen saturation and the total hemoglobin concentration of the surrounding blood vessels of a brain tumor in an immunocompromised nude mouse. This exemplified the ability of photoacoustics to reveal hypoxia in tumor neovasculature, which may play a role in future applications of determining characteristics associated with tumor induced hypoxia and aid in determining the most effective type and timing of therapy³⁰.

An area of great interest in photoacoustics lies within noninvasive imaging of the cerebral cortex. *Yang* et al. performed a review of nanoparticles that play a

beneficial role in photoacoustics and were able to demonstrate an increase in the NIR contrast of cortical blood vessels in the *in vivo* rat brain. Nanoshells comprised of PEGylated surfaces were inoculated into the tail vein of Sprague-Dawley rats. Successive images were acquired over a period of three injections of the nanoshells, which allowed quantification of circulation dynamics in the cortical blood stream. Comparing pre- and post-injection images, a sharp increase in contrast of cortical vasculature was visible as well as a 63 % in blood vessel absorption. This work illustrated the ability of photoacoustics to visualize and measure cortical blood volume in noninvasive studies of brain function⁴⁷.

3 PAM System

3.1 Control System

A PC with a custom built LabVIEW application controlled the data acquisition unit and the motion axes needed for imaging via 3-D mechanical scanning. The LabVIEW control system is a simple state-machine as seen in Fig. 3.1. Stepping through the execution, default values are passed to the GaGe card in order to initialize needed attributes and data files are created to hold the collected data. The bounds of the scan are passed to the motion axis system via the graphical user interface. From there, firing of the laser commences and raster scanning takes place. Once the laser is active and scanning is underway the control system alternates between the states of bounds checking (i.e. are we still within the scanning region of interest), data collection, and whether or not to continue the scan. More specifically, as one raster scan takes place, the states that are executed go from (a), which checks to verify that we are within our bounds for this scan along the x-axis. If true, data is collected and motion along the x-axis continues (b), afterwards a state transition is made back to (a). If false (i.e. we have moved beyond our x-axis bound), then a state transition is made to (c), which establishes

whether or not the scan is still within the y-axis bounds. If true, then a state transition is made back to (a) since there still exists area in our ROI to scan, and the execution continues. If false we know we have completed our scan, files are closed, and the system is halted.

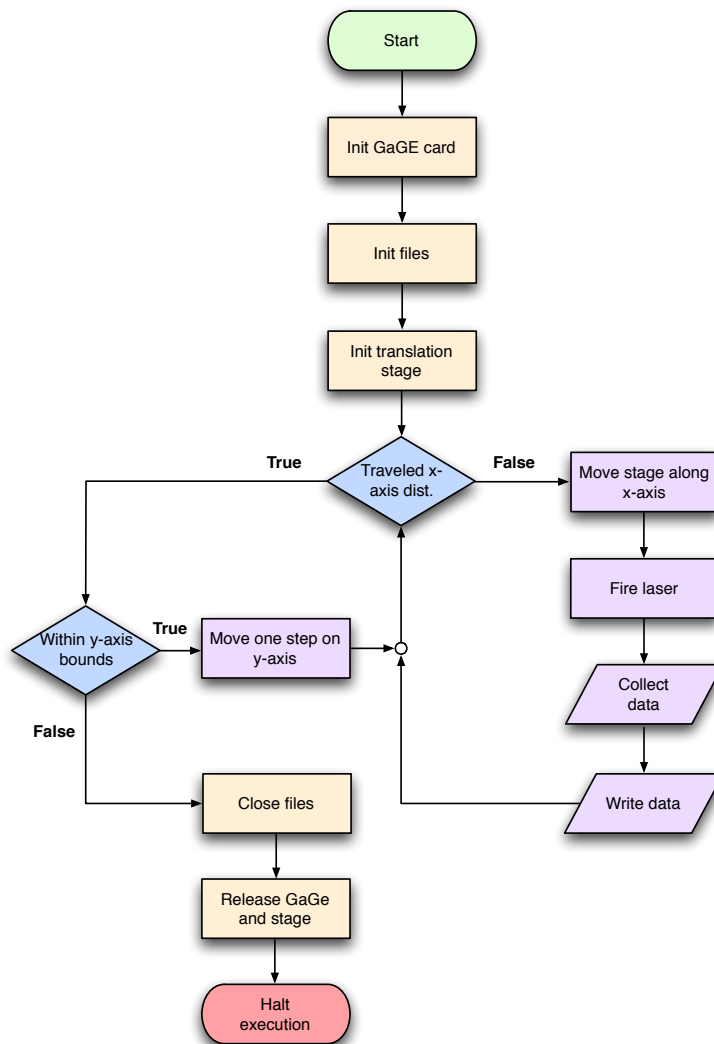


Figure 3.1: Flowchart depicting the state-machine of the LabVIEW control system.

3.2 Dark-field PAM

A diagram of the experimental setup for the PAI system is shown in Fig. 3.2. A 25 MHz focused ultrasound transducer (13-2506-R, Olympus-NDT, Waltham, MA), with a focal depth of 15 mm and an aperture size of 9.4 mm, captures the photoacoustically generated waves. The transducer exhibits lateral and axial resolutions of 150 μm and 100 μm , respectively, with 61% -6-dB fractional bandwidth. The signal from the transducer is delivered to a pre-amplifier (5072PR, Olympus-NDT, Waltham, MA), and finally collected by a personal computer through an A/D data acquisition card (CS21G8-256MS, GaGe, Lockport, IL). The ROI of the mouse is placed below the membrane of a water tank and the 3-D positioning stage is adjusted to place the confocal region over the ROI. Ultrasound gel is placed between the surface of the mouse and the membrane of the water tank in order to couple mouse and membrane, which permits acoustic waves to pass through the juncture and make their way to the transducer for recording.

The Q-switched Nd:YAG laser (Continuum Surelite, 5 ns pulses, 10 Hz pulse repetition) pumps a tunable OPO laser (Surelite OPO PLUS) with the output steered through a series of prisms to a conical lens. The conical lens produces annular illumination, which is focused into the sample via an optical condenser. At the tissue surface, the ring has a diameter of ~ 5 mm. The condenser is used to create a dark-field illumination pattern that reduces the fluence at the surface

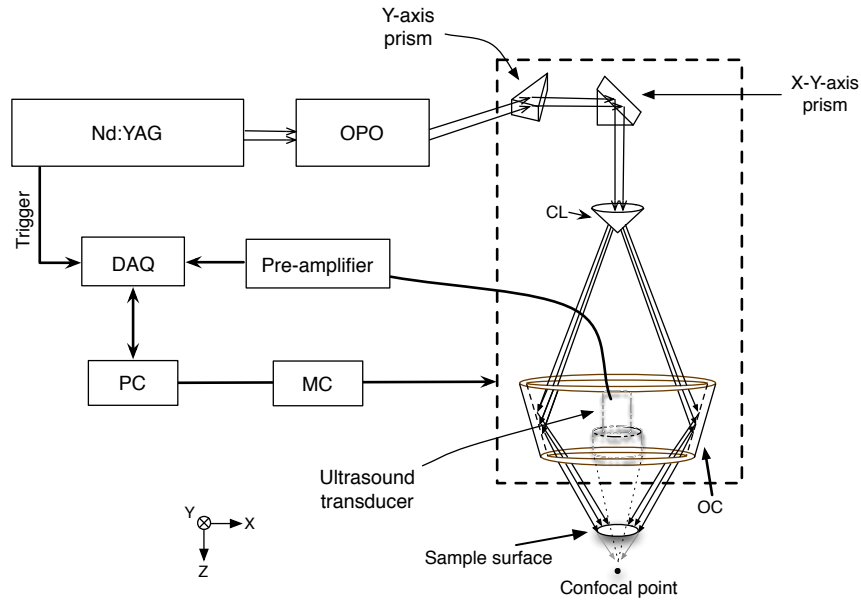


Figure 3.2: PAM imaging system hardware diagram. (CL) conical lens; (MC) motor control; (OC) optical condenser.

of the specimen, which in turn reduces signals from the skin surface that might overpower underlying PA signals of interest^{48,17}. The photoacoustic images are obtained by mechanically raster scanning the ROI using lateral and vertical step sizes particular to a given experiment. At each position in the scan the incident pulsed laser light irradiates the sample and the acoustic response, gathered from the transducer and pre-amplified, is recorded via the data acquisition card at a sampling rate of 500 MHz. Sampling is initiated by the trigger signal from the laser source at each acquisition position.

4 Subcutaneous malignant melanoma in the *in vivo* mouse model

Knowledge of the depth, proliferation, and shape of malignant melanoma are critical in determining clinical prognosis of the disease. Currently, depth and thickness serve as guiding attributes in staging classification and treatment decisions. PAM, with its ability to separate responses from various tissues based on their varying molar extinction spectra, is highly suited for application in melanoma imaging. This chapter presents results obtained from applying two optical wavelengths (532 and 764 nm) to *in vivo* subcutaneous malignant melanoma in order to image vasculature and tumor profiles (depth, shape, and thickness) using the B16F10 murine melanoma cell line in live BALB/c mice.

4.1 Introduction

Current clinical practice utilizes incisional or excisional biopsies in order to obtain knowledge pertaining to the status of melanoma tumors. These invasive procedures often leave the patient with pain and visible scars post biopsy. Non-invasive imaging techniques such as PAM have the potential to remove these undesirable outcomes while still providing physicians with the ability to diagnose

and monitor tumors during treatment.

Various imaging technologies have been investigated as possible noninvasive methods as discussed in section 1.4, however each of these has unavoidable limitations that prevent their sole use as imaging techniques for subcutaneous melanoma. These drawbacks range from insufficient penetration depth, which removes the possibility of measuring tumor thickness, to poor contrast and spatial resolution. PAM mitigates the lack of penetration depth and improves contrast and spatial resolution, thus yielding a superior technique with respect to imaging subcutaneous melanoma.

4.2 Materials and Methods

Subcutaneous injections

In order to bypass the prolonged staging of melanoma growth and exercise the depth potential of PAM, growth of the melanoma was initiated in the subcutaneous layer through direct delivery of tumor cells as seen in Fig. 4.1. More specifically, B16F10 tumor cells were harvested from culture and resuspended at a concentration of 5×10^3 cells/ μ L. Hair covering the hip of the mice were removed using a depilatory cream (Nair) in order to expose the skin. Following hair removal 100 μ L of the solution was injected, under isoflurane anesthesia, subcutaneously in the hip of the hind leg of female BALB/c mice (Harlan Sprague Dawley Inc., ~25 g). The

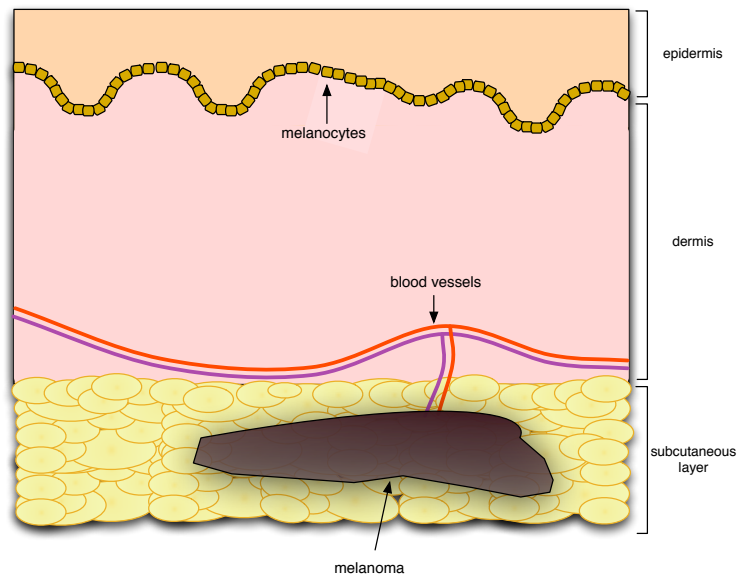


Figure 4.1: Anatomy of melanoma growth after subcutaneous delivery of B16F10 melanoma cells.

cell line used demonstrated rapid and aggressive growth, therefore an incubation period of only 3-4 days was used to allow adequate tumor formation. After the incubation period tumors averaged $\sim 10 \times 5$ mm with an approximate thickness of 1.5 mm. Growth of the subcutaneous melanoma was irregularly shaped and often proliferated into the dermis, but never crossed into the epidermis.

Tail vein injections

Tail vein injections were administered to systemically deliver tumor cells and facilitate metastatic tumor growth. The same strain of mice, tumor cell line, and volume of cells were administered via tail injection as given for subcutaneous hip

inoculation. Mice were inspected daily in order to observe visual cues demonstrating metastatic tumors (visible tumors, weight loss, etc.). However, tail injections required significantly more incubation time for noticeable melanoma growth to occur. Due to the administration method of the tumor cells into the circulatory system, tumor growth was free to commence systemically, which often produced tumor growth in the lungs leading to rapid weight loss in the specimen once the tumors had formed. Therefore, the incubation period was typically limited to a timeframe of ~ 2 weeks.

4.3 Results and Discussion

In this work, images of metastatic and primary subcutaneous melanomas were captured, as well as their accompanying angiogenic vasculature. Two optical wavelengths were used in the hip tumor (Fig. 4.2), 532 and 764 nm. However, 532 nm was exclusively used with the metastatic tumor found on the spine (Fig. 4.3). The maximum operating energy level of $\sim 5 \text{ mJ/cm}^2$ was used for both tumors. Using 532 nm wavelength, PAM is able to image both the melanoma tumor as well as the surrounding vasculature because of the comparably high absorption of hemoglobin and melanin in this visible spectral region. However, if the tumor is of sufficient thickness, 532 nm has difficulty penetrating through the melanin rich tumor. In order to overcome this limitation, PAM has the ability to operate at varying wavelengths, which in turn have varying molar extinction coefficients in

tissue. This allows incident light to infiltrate the tumor due to decreased absorption of melanin and hemoglobin at wavelengths that exist further in the region of the NIR spectrum. The results from the combination of two separate wavelengths can be seen in Fig. 4.2(c).

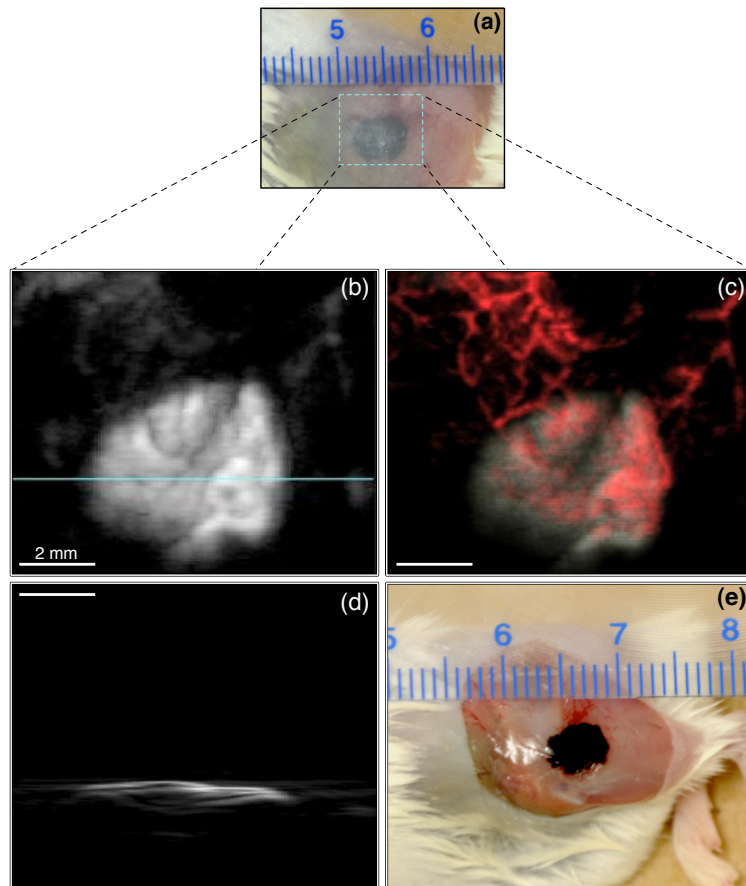


Figure 4.2: Anatomical and PA images of a subcutaneous melanoma *in vivo*. a) Noninvasive anatomical photograph showing the bounded ROI; b) image acquired at 764 nm optical wavelength; c) composite image acquired at 532 nm and 764 nm optical wavelengths; d) cross-sectional image corresponding to the line in b) at 764 nm optical wavelength. Scale bars are the same for all three images.

Looking at Fig. 4.2(a) we can see the anatomical view of the subcutaneous tumor residing *in vivo* in the hip of a live BALB/c mouse pre-imaging. The MAP of the x - y plane is shown in Fig. 4.2(b), demonstrating the results of applying 764 nm wavelength to the bounded region in Fig. 4.2(a). The image produced at 764 nm demonstrates the shape and contours of the tumor, while simultaneously removing the majority of the results from the surrounding arterioles and venules. Fig. 4.2(c) shows the composite image, where tumor region obtained at 764 nm is pseudo-colored grey and blood vessels captured from 532 nm are pseudo-colored red. Fig. 4.2(d) shows the B-scan from the horizontal line in Fig. 4.2(b), demonstrating the thickness profile of the melanoma, which was found to be ~ 1.0 mm. Comparing the invasive anatomical photograph in Fig. 4.2(e) with the MAP and composite image, it is clear that PAM accurately imaged vasculature as well as tumor.

The images in Fig. 4.3 depict the results from using 532 nm optical wavelength to image a metastatic tumor residing above the spine in a BALB/c mouse. In Fig. 4.3(a) we clearly see the tumor along with surrounding blood vessels. Fig. 4.3(b) shows the B-scan along the green line in Fig. 4.3(a), which demonstrates the thickness of the tumor as well as the diameter. The tumor was found to be ~ 3 mm in diameter. Despite a small amount of noise from background tissue, we see a lack of any response from the spine itself that resides directly below the tumor, which confirms that we are able to selectively target and differentiate the tumor from surround

tissue and structures. This result is vital when performing *in vivo* imaging as it provides a means to accurately discern cancerous tissue from normal healthy tissue and mitigates the impact of interference of the two with one another, thus providing clear images that depict areas of concern.

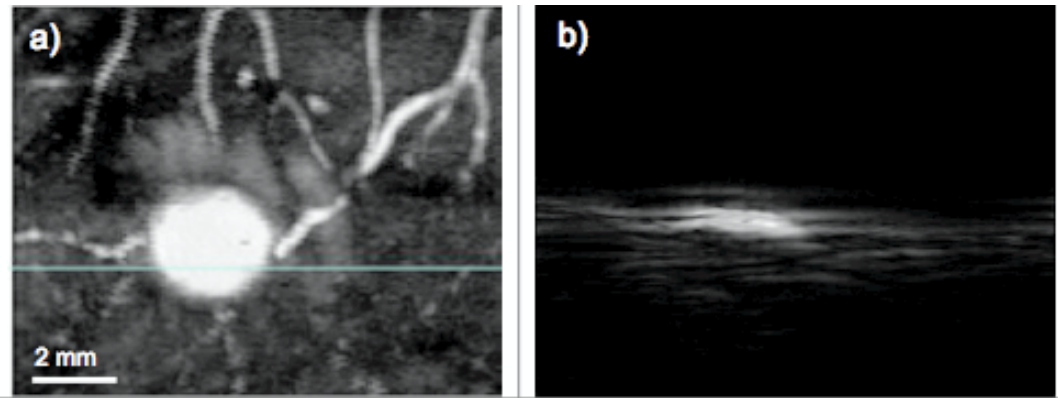


Figure 4.3: PA images of a metastatic melanoma on the spine. a) PA image at 532 nm optical wavelength; b) cross-sectional image corresponding to the line in a). Scale bars are the same for the two images.

4.4 Conclusions

PAM's ability to differentiate and target tissues and manifestations of interest by varying the optical wavelength was demonstrated. It was shown that PAM can be used to accurately image local melanoma tumors and vasculature as well as metastatic arising tumors while maintaining clarity and limiting interference from surrounding biological structures of non-interest. These results suggest that PAM can potentially be used in a clinical setting in order to provide critical diagnosis

and prognosis information.

5 Photoacoustic Discrimination of Malignant Melanoma Using NIR-dye as Contrast Agent

The use of a contrast agent with photoacoustic imaging of malignant melanoma greatly enhances the differentiation between tumorous region, dye, and surrounding tissue. Use of a contrast agent also provides the possibility of encapsulation within nanoparticles, enabling targeted delivery to cancer cells and the ability to track them, which is suggested for early detection of malignant tumors^{49,50}. Under in vivo conditions a NIR-dye (IR-27, absorbance peak - 988 nm) was subcutaneously injected adjacent to an existing melanoma carcinoma grown in a BALB/c mouse. The region was imaged at two separate wavelengths, 764 nm and 988 nm. Maximum amplitude projection images were obtained that demonstrated visible regions of tumor and dye at 764 nm and only dye at 988 nm. Our results demonstrate effective use of IR-27 dye as a contrast agent in differentiation between malignant melanoma and NIR-dye under photoacoustic imaging.

5.1 Introduction

Currently there does not exist a method to successfully differentiate malignant melanoma from benign melanoma using photoacoustic techniques. Current re-

search has shown an effective approach of utilizing various contrast agents to improve contrast of photoacoustic images and target specific pathologies such as cancerous tumors^{43,51,30,52-54}. However, to the best of our knowledge there has yet been research to investigate the capabilities of utilizing a NIR-dye in deciphering the state of tumorous growth (i.e. malignant vs. benign) using PAM.

The use of contrast agents greatly enhances the magnitude of electromagnetic absorption, which is ideal for photoacoustic applications targeting specific pathologies such as malignant melanoma. Contrast agents in the form of NIR-dyes allow optical absorption to occur at levels deeper within tissue since peak absorption occurs in the NIR region where attenuation of the optical signal is low. However, the greatest benefit of using PAM with the IR-27 dye is found in the differing molar absorptivity of melanoma and dye, allowing for near complete removal of the signal obtained from melanoma, i.e. a severe reduction in the absorbance of light by the carcinoma, by simply altering the wavelength of the incident optical source.

When NIR-dyes undergo optical absorption, electrons within the molecules of the dye jump to excited states, and subsequently dissipate energy in two ways of interest within our application - heating, which yields thermoelastic expansion, and fluorescence. The pathway that is of interest to photoacoustics is absorption and thermoelastic expansion, which produces the acoustic signal that relates information about the absorber. The second pathway is radiative (i.e. fluorescence).

Looking at total energy conservation, it is apparent that the energy that does not fluoresce contributes to the photoacoustic signal. Therefore we can conclude that the greater the fluorescence of the dye, the smaller the resultant photoacoustic signal, and conversely the less the dye fluoresces the larger the heat pathway, which leads to improved thermoelastic expansion and acoustic wave generation.

5.2 Materials and Methods

The NIR-dye, IR-27 (peak absorbance - 988 nm), was obtained from Sigma-Aldrich. The dye was dissolved in sterile DMSO producing a concentration of 2.55 mg/mL and stored at -30 degrees C. The B16F10 murine melanoma cell line was subcutaneously injected into the hind leg of a live BALB/c mouse (Harlan Sprague Dawley Inc., ~30 g). The tumor cells were allowed a four day incubation period in order to facilitate growth of a tumor of adequate size. The cell line produced a resulting tumor of dimensions 7 X 2 mm. Once the tumor was verified to be of sufficient size, approximately 20 μ L of the solution was subcutaneously injected into the hind leg of a deceased BALB/c mouse producing a 5 X 2 mm deposit. The injected dye solution was administered adjacent to the melanoma tumor, allowing for easy comparison between the regions as seen in Fig. 5.1.

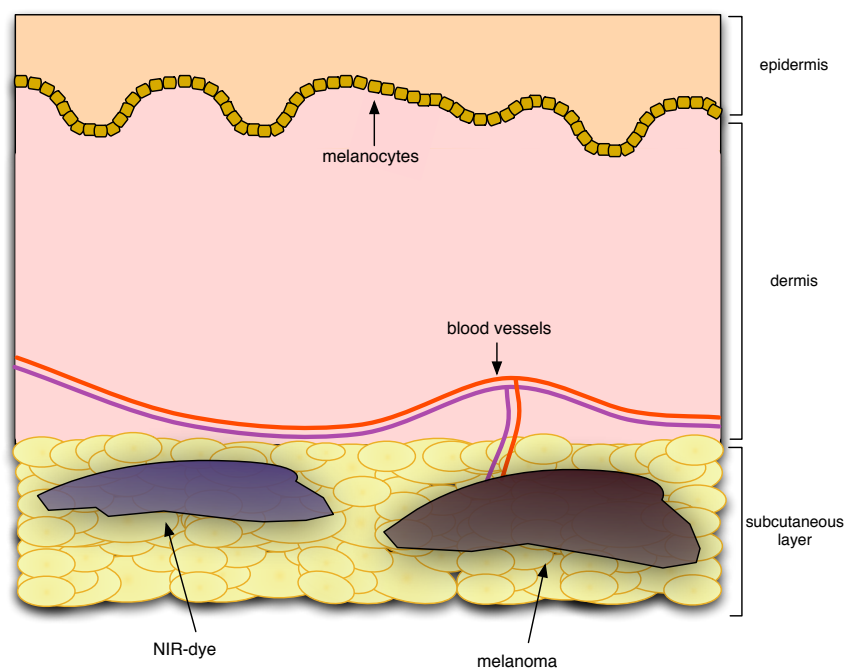


Figure 5.1: NIR-dye depot and melanoma tumor. Dye and tumor are located proximally in the subcutaneous layer in the hind leg of a BALB/c mouse.

5.3 Results and Discussion

Using a dark-field PAM system described in chapter 3 in conjunction with the aforementioned focused 25 MHz transducer, noninvasive *in vivo* imaging of melanoma and NIR-dye was achieved. An Nd:YAG laser operating with a pulse width of 5 ns and repetition rate of 10 Hz pumped an OPO to yield wavelengths of 764 and 988 nm for each respective scan. Incident light on the surface of the ROI was held to $< 4 \text{ mJ/cm}^2$ with respect to both wavelengths used in the study. Post inoculation of NIR-dye, and prior to imaging, the mouse was sacrificed in order to

remove any chance of motion artifacts arising during the imaging procedure.

Fig. 5.2(a) shows the first scan over the ROI using 764 nm optical wavelength. We can clearly see the tumor region (bounded area) as well as the dye deposit in the image, revealing that dye and tumor exhibit large thermoelastic responses at 764 nm wavelength and are clearly discernible from one another due to their anatomical locations.

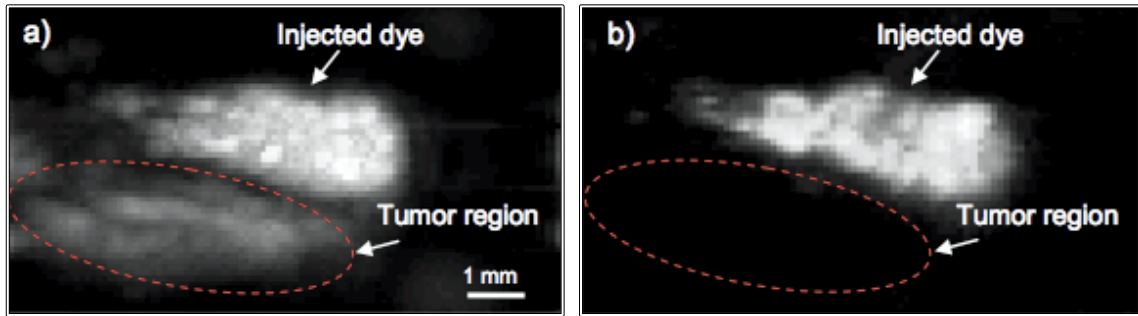


Figure 5.2: PA images comparing dye and tumor using 764 nm and 988 nm wavelengths. a) Image acquired at 764 nm wavelength. b) Image acquired at 988 nm wavelength.

Increasing the wavelength to 988 nm produced the image in Fig. 5.2(b) with the noticeable lack of tumor in the bounded region. This absence of tumor response arises due to the fact that the optical wavelength of 988 nm produces an acoustic response from the NIR-dye that dominates the response from the tumor. More specifically, energy absorption from incident light with respect to the tumor is highly reduced at 988 nm when compared to 764 nm, leaving us with only the discernible response from the dye. To further illustrate the responses from the

differing wavelengths we can look at Fig. 5.3. Fig. 5.3(a),(b) represent normalized intensity plots of B-scans through the same location of the mouse, with their respective wavelength. We see in Fig. 5.3(a) that the response from tumor and dye are decipherable from one another, and moreover both responses are present. This is contrasted by Fig. 5.3(b), in which only the response for the dye is present and there is a noticeable lack of response from the tumorous region. It should be noted that the regional locations of both B-scans for both wavelengths was held constant in order to accurately compare the responses. At 988 nm wavelength the maximum intensity of dye to tumor produced a gain of 24dB. When comparing maximum intensities from the tumor at both wavelengths, we find that the result from 988 nm yields a gain of -12dB with respect to 764 nm, thus providing quantitative information demonstrating an attenuated response from the tumor at 988 nm.

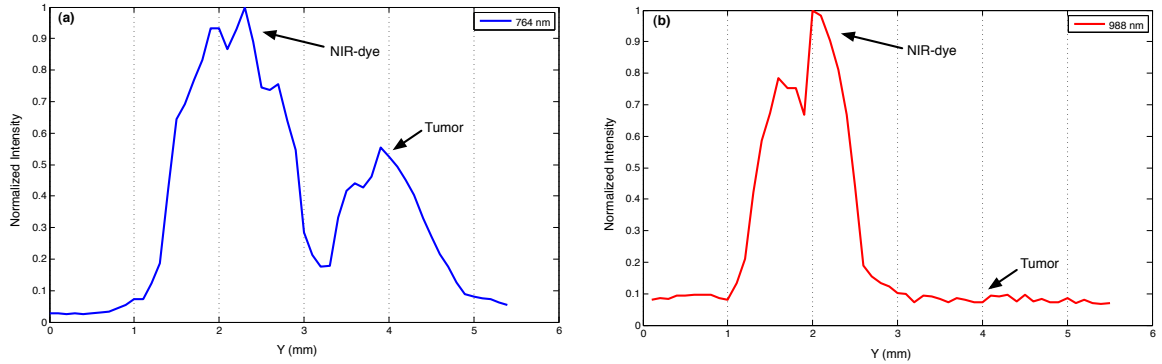


Figure 5.3: Normalized intensity plots of B-scans at 764 nm and 988 nm. (a) Plot of B-scan at 764 nm wavelength. (b) Plot of B-scan at 988 nm wavelength. Both B-scan plots represent the same location.

The domination of the dye compared to tumor in Fig. 5.3(b) can be explained by the dye's higher molar absorptivity than the tumor at 988 nm. This also holds with respect to the tumorous region at both wavelengths - 764 and 988 nm. More specifically, the molar absorptivity of the tumor has a relative peak value at 764 nm when compared to other absorbing chromophores and diminishes as the wavelength moves higher into the spectrum. This exemplifies the fact that it is possible to target specific areas of interest by using contrast agents and varying optical wavelengths.

5.4 Conclusions

In summary, photoacoustic differentiation of NIR-dye and melanoma tumor has been implemented noninvasively. This technique provided an accurate and noninvasive method to delineate tumor and contrast agent from surrounding tissue. The possibility of extending this work is of significant interest. For example, contrast agents are easily conjugated with proteins, antibodies, drugs, and other bioactive agents. This technique has the potential to be extended to such areas, enabling noninvasive detection of drug/dye encapsulated particles to melanoma tumors, and providing a means to track the efficacy and delivery of such agents *in vivo*.

6 Noninvasive Photoacoustic Microscopy of Brain Tumors in Live Mice

* Chapter has been submitted to the *Journal of Biomedical Optics*

Noninvasive photoacoustic microscopy (PAM) is a promising imaging modality for detecting and imaging brain tumors in experimental models. The fusion of optics and ultrasound coupled with the intrinsic optical absorption properties of tumors and associated vasculature give rise to detailed images and invaluable information of the current status of the disease. Here we present for the first time, to the best of our knowledge, the application of PAM applied to in vivo imaging of melanoma brain tumors in live mice. Utilizing the fact that NIR light has a deep penetration depth and is able to pass through skin and skull, making its way into brain tissue, we were able to accurately detect, image, and track melanoma tumor growth in the brain of BALB/c mice.

6.1 Introduction

Photoacoustic microscopy is becoming an established imaging modality in the field of biomedical imaging^{19,41,24,25,28,26}. Following ANSI set guidelines for acceptable operating parameters, PAM is deemed safe for use with human and animal models. A wide range of work has been previously accomplished us-

ing photoacoustic imaging (PAI), ranging from imaging neonatal brains,²⁷ burn depth estimation,⁷ vascular and hemodynamic measurements,^{45,24,46} and various oncology imaging applications.^{44,33,17,19}

Melanoma is one of the most lethal cancers and currently represents a significant public health problem in the United States. For patients with stage IV melanoma, the incidence of brain metastases has been reported to be 10% to 40%, making melanoma the third most common metastatic brain tumor in the United States, following lung cancer and breast cancer⁵⁵. With effective treatments, survival time following central nervous system (CNS) metastases is between 2 and 5 months^{56–59}. Without treatments, most patients show enhanced deterioration and ultimately death. Recognition of the initiation and progression of melanoma brain metastases in experimental models is necessary to identify new research strategies useful for the diagnosis and subsequent therapy of these tumors in humans. Hence, in vivo monitoring of the formation and growth of melanoma tumors in live brain could have major implications for the design of improved therapies.

Recent mouse models have been developed that allow controlled study of various diseases that mimic those found in humans. These models provide an excellent setting for translatable research to humans in hopes of providing clinically relevant breakthroughs. Currently a model allowing for the growth and proliferation of brain tumors created from the B16F10 murine melanoma cell line has been established. Utilizing the varying molar absorptivity that is innate to specific biological

tissue, PAM can easily discern melanoma tumor growth from surrounding vasculature and soft tissue yielding high contrast and excellent spatial resolution, thus making it highly suited for application in brain tumor imaging in the mouse model³³. Because PA wave generation arises from diffuse photon absorption and the resultant signal of interest is acoustic, PAM has the ability to overcome light scattering and attenuation that arises from skull and scalp that typically inhibits other purely optical imaging modalities⁶⁰.

6.2 Materials and Methods

PAM System

Our photoacoustic imaging system is identical to the one presented by *Song et al.* for deep PA imaging²¹. The system consists of an ultrasound transducer, a laser system, and receiving electronics. A Q-switched Nd:YAG laser (Surelite; Continuum, Santa Clara, CA) was used to pump a tunable OPO laser (Surelite OPO PLUS; Continuum, Santa Clara, CA) to obtain a 764 nm wavelength laser with a 10-Hz pulse repetition rate. The produced laser light forms a ring shape illumination after passing through several prisms and a conical lens and then is refocused inside the tissue sample by an optical condenser. At the tissue surface, the ring has a diameter of ~ 5 mm. The subsequently generated ultrasonic waves are detected by a focused ultrasonic transducer (13-2506-R, Olympus-NDT,

Waltham, MA), delivered to a pre-amplifier (5072PR, Olympus-NDT, Waltham, MA), and finally collected by a personal computer through an A/D Scope Card (CS21G8-256MS, Gage, Lockport, IL). The ultrasound transducer (15 mm focal length; 9.4 mm aperture size) has a central frequency of 25-MHz with 61% -6-dB fractional bandwidth and exhibits lateral resolution of 150 μm and axial resolution of 100 μm when used for photoacoustic imaging.

Inoculation of Melanoma Cell Line Intracerebrally

B16F10 melanoma tumor cells grown in DMEM supplemented by 10% fetal bovine serum, 1% penicillin, and 1% streptomycin were harvested by trypsinization, washed in 1x phosphate-buffered saline, resuspended in 1x phosphate-buffered saline at a concentration of 2,500 cells/ μL , and kept on ice until injected intracranially. BALB/c mice (Harlan Sprague Dawley Inc., ~22 g) were deeply anesthetized using a cocktail of 83 mg/kg of ketamine and 17 mg/kg of xylazine, which was intraperitoneally injected. Hair covering the scalp of the mice were removed using a depilatory cream (Nair) in order to expose the skin. Following hair removal mice were secured in a small animal stereotactic frame. Following liquid tear application to the eyes to prevent ocular damage during anesthesia, povidone iodine was applied on the skin covering the skull around the anticipated midline incision site, and an alcohol pad was then used to wipe down the skin to remove excess povidone iodine and provide further sterilization. A ~1 cm incision

on the midline of the skull was made to expose the calvarium, and a burr hole was drilled 1 mm anterior and 2 mm lateral (right) from the bregma by a Dremel 10.8V 8000-03 with a rounded high speed cutter bit, producing a burr hole ~ 1 mm in diameter as seen in Fig.6.1.

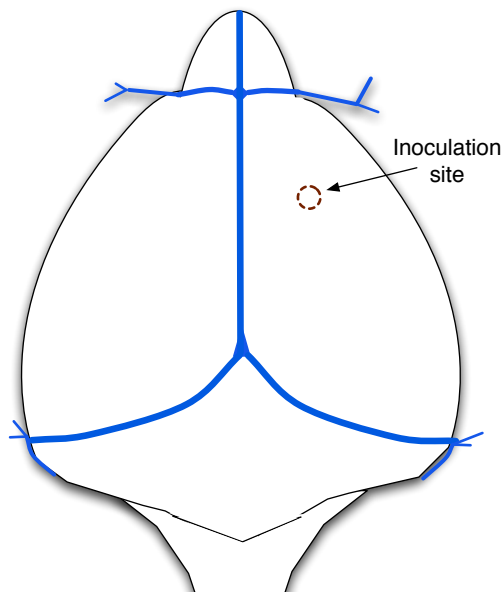


Figure 6.1: Site of inoculation of B16F10 tumor cells in the *in vivo* mouse brain.

A 10 μ L blunt-tipped Hamilton syringe loaded with 2 μ L was lowered into the hole 3.3 mm from the cortical surface but retracted 0.3 mm to form a small pocket for the liquid to be injected, thereby introducing the cells into the right basal ganglia. The B16F10 cells were injected into the brain at a speed of 0.4 μ L/minute and a total volume of 2 μ L (5,000 cells injected per mouse). The syringe was left in place for ~ 1 minute following tumor cell injection to allow for pressure stabilization.

After the intracranial injection, each animal was removed from the stereotactic frame, and the incision was closed with an absorbable surgical suture. Triple antibiotic ointment was added to the incision to help further prevent infection, and the animals were slowly warmed on a heating pad and monitored until they awakened. All in vivo procedures were carried out following the guidelines of the University of Kansas Institutional Animal Care and Use Committee (IACUC).

Image Acquisition

Photoacoustic images of the brain melanoma were first acquired on the fifth day after the tumor cell injection. During the photoacoustic imaging, a mouse bearing with melanoma brain tumor was initially anesthetized with a mixture of 87 mg/kg ketamine and 13 mg/kg xylazine, and then the anesthesia was maintained with the inhalation of a mixture of pure oxygen and 1% isoflurane. The brain region where the melanoma cells were injected was imaged. The same process was repeated in the following days, and size increase of the brain melanoma tumor due to the growth of the brain melanoma tumor can be directly indicated from the PA images. The animals showed classic signs of morbidity approximately two weeks following the tumor injections.

6.3 Results and Discussion

Using the 25 MHz ultrasonic transducer previously mentioned in conjunction with 764 nm wavelength operating at $\sim 10 \text{ mJ/cm}^2$, PAM was used to noninvasively image a melanoma tumor residing in the cortical region of live mice. Data was captured by raster scanning the region of interest, an $11 \times 11 \text{ mm}$ area on the surface of the scalp. As a result of the inoculation procedure, scalp wounds persisted during the life span of the mice, which increased the levels of energy absorption on the scalp surface during imaging. To overcome the large acoustic response from the wounds, post-processing of the data was employed to remove surface wound response similar to methods demonstrated by *Zhang et al.*⁶¹.

Mouse *A* was imaged at day 3 and day 9 post-inoculation of the melanoma cell line. Fig. 6.2 clearly demonstrates the progression of the tumor growth in mouse *A* over a period of 6 days in the same bounded region over the time period. Fig. 6.2(a) gives an invasive anatomical view of the tumor growth that occurred over the 9 day period within the brain of the specimen. When looking at the MAP image In Fig. 6.2(b), specifically within the bounded region, we see a minimal acoustic response within the bounded region denoting a lack of an absorber, i.e. a tumor. Figure. 6.2(b) reveals that tumor growth has yet to proliferate within the region and currently yields almost no acoustic response from the area. Allowing the tumor cells a timeframe of 6 days to mature and produce a tumor of sufficient

size lead to results found in Fig. 6.2(c). Looking at Fig. 6.2(c), again within the bounded region, we can see the distinguishing shape of a melanoma tumor present within the same bounded location as Fig. 6.2(b), which lacked any sufficient tumor growth. Comparing Fig. 6.2(a) with Fig. 6.2(c), it is clear that the PAM image clearly identifies the tumor and agrees with the anatomical photograph taken after image acquisition, thus providing a clear picture of growth and proliferation of the injected cell line into a tumor.

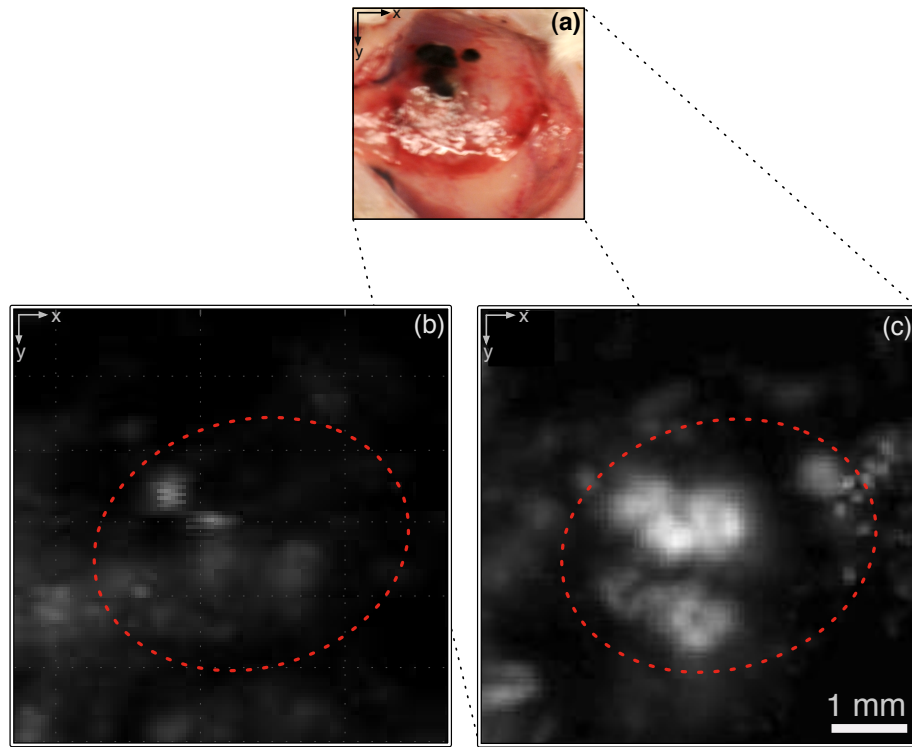


Figure 6.2: Noninvasive *in vivo* PAM images of mouse A over a period of 6 days. (a) Photograph taken after image acquisition and scalp and skull removal. (b) 3 days post-inoculation of the melanoma cell line. (c) Same region in (b) imaged 9 days post-inoculation. Scale bar is the same for both images.

To further highlight the disparity and evolution in tumor growth between day 3 and day 9 in mouse *A* the maximum amplitude projections of the tumorous region are shown in 3D-space in Fig. 6.3(a)(b), and (c)(d), respectively. On day 3 we see very little uniform response from the bounded region verified by the 3D-projection. It is clear the tumor has yet to mature after 3 days and the response we see is intermixed with background noise. On day 9 the 3D-projection demonstrates a clear pattern emerging from the tumor. The overall shape and dimensions are visible and we can see a uniform response from the acoustic signal as the pattern of tumor growth becomes more discernible. At day 9 it is possible to distinguish tumor from background noise due to the dominance of absorbance by the melanoma at this stage.

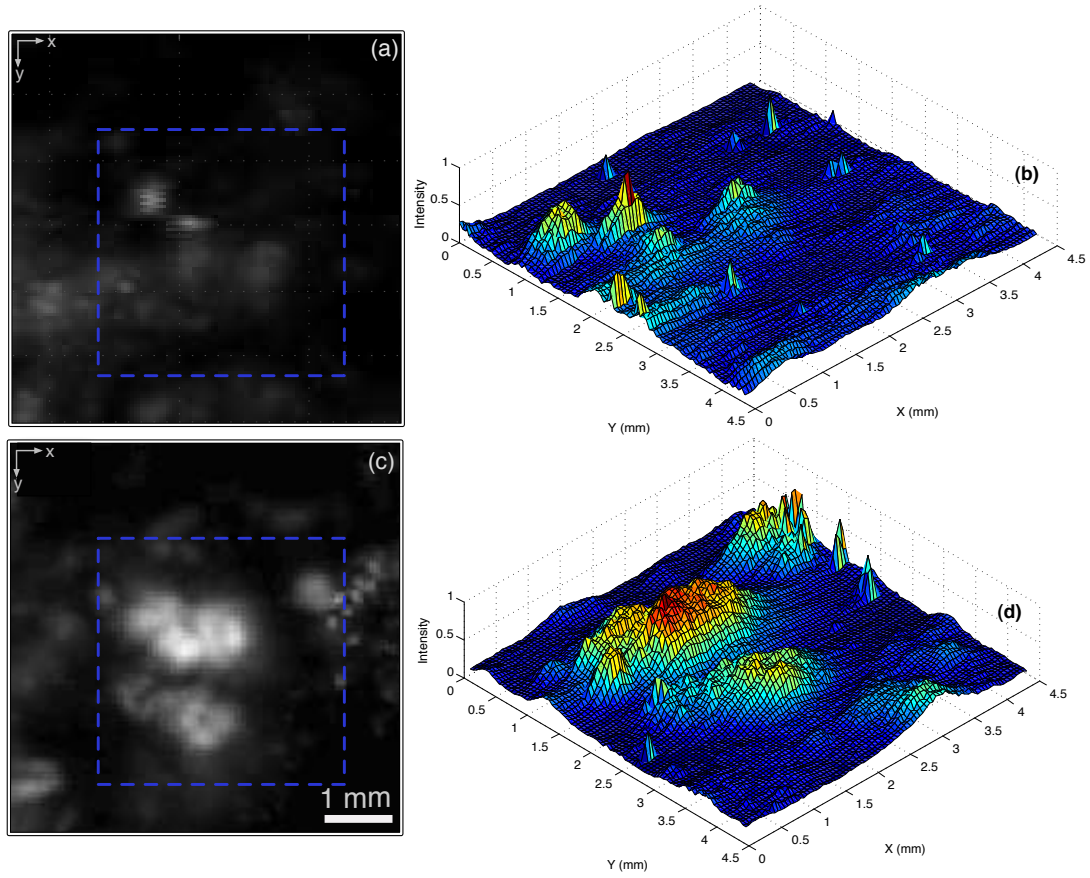


Figure 6.3: Comparison of maximum amplitude projections in 3D-space over a timeframe of 6 days. (a) MAP at day 3. (b) MAP of bounded-region of (a) in 3D-space. (c) MAP at day 9. (d) MAP of bounded-region of (c) in 3D-space.

The thickness profile of the tumor bearing mouse *A* is shown by the B-scans in Fig. 6.4(c)-(d). Here we see Fig. 6.4(c), which represents the B-scan shown by the horizontal green line running from left to right in (b), showing a tumor thickness of ~ 1.5 mm. Fig. 6.4(d) contains the B-scan shown by the blue vertical line, running from top to bottom in (b). When looking at (d) we see that depth of the tumor varies, as well as the thickness, over the region of growth. In both B-scans it is

possible to distinguish brain tumor signals from background noise and accurately assess tumor location, thickness, and growth patterns.

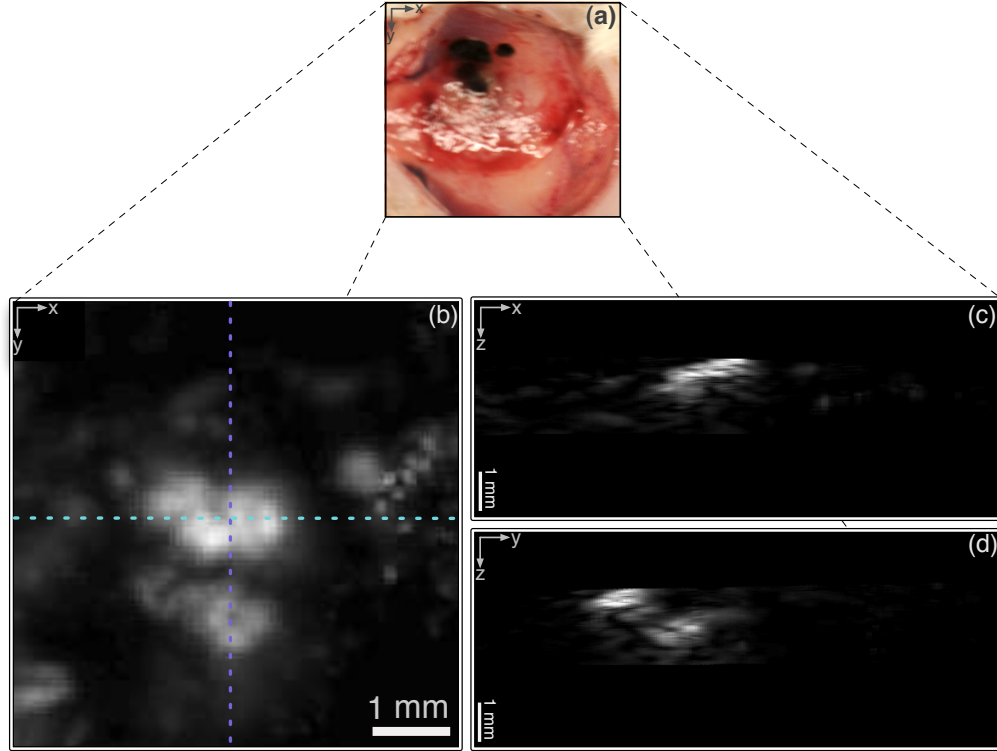


Figure 6.4: B-scan of tumor in mouse *A* at day 9 post-inoculation. (a) Photograph taken after PAM image acquisition and scalp and skull removal. (b) MAP image of the region in (a); formed while scalp and skull were intact. (c) Horizontal B-scan along the green line in (b). (d) Vertical B-scan along the blue line in (b). Scale bar is the same in all images.

Fig. 6.5 (a)-(e) were taken from experimental mouse *B* on day 5, day 8, day 10, day 13 and day 14 after the injection of tumor cells, respectively. On day 5 and day 8, the brain tumor signals are fairly weak and do not distinguished from background because the tumor is still small. On day 10, the PA signals from the

melanoma brain tumor becomes dominate. The size of the brain melanoma tumor shown on the PA image shows the significant enlargement as the tumor continues to grow over the last two days before morbidity.

The corresponding B-scan photoacoustic images of the melanoma tumor from the same mouse are in Fig. 6.5 (f)-(j). These clearly show the depth of the melanoma tumor in the mouse brain on the five separate imaging days after injection. The brain melanoma was initially located about 2-3 mm deep underneath the skull. As the time elapses, the thickness of the melanoma tumor increases. In the 14th day, the mouse died from the brain melanoma and the open skull photograph was taken and shown in Fig. 6.5 (k). The final size of the tumor is about 4 mm in diameter inside the brain.

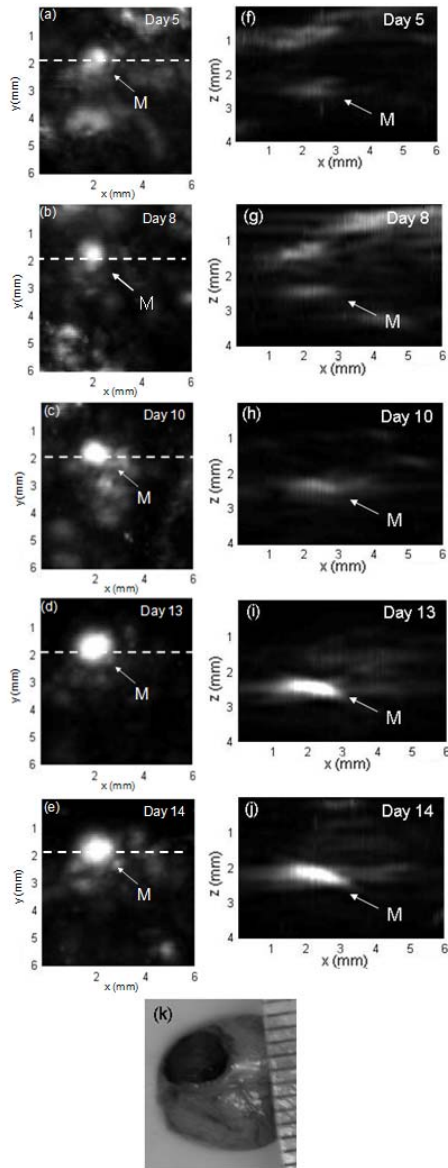


Figure 6.5: Noninvasive MAP images of the brain melanoma in day 5 (a), day 8 (b), day 10 (c), day 13 (d), day 14 (e) after the injection of tumor cells, respectively. (f)-(j) The B-scan images corresponding to the dashed lines in (a)-(e), respectively. (k) Invasive anatomical photograph after the mouse death. All PA images are in the same intensity scale. M: melanoma brain tumor.

Both the size and depth information of the brain tumors are important in planning and verifying the treatment of primary brain tumors (e.g., glioma). This study showed PAM can monitor the brain tumor growth inside a small animal's brain noninvasively, and therefore, photoacoustic imaging is capable of being as an imaging tool to *in vivo* track the response of the brain tumor to therapies.

6.4 Conclusions

In summary, both the size and depth information of the brain tumors are important in planning and verifying the treatment of primary brain tumors (e.g. glioma). We have shown the ability of a reflection-mode dark-field PAM system to detect, image, and track the progress of melanoma tumors noninvasively in a metastasis model. PAM of malignant melanoma can potentially provide and/or enhance current diagnostic techniques and offer an accurate noninvasive method to monitor cancer progression in biological samples. Looking at the results produced in this study, we feel PAM has a strong future in the area of oncology research.

Bibliography

- [1] L.V. Wang. Ultrasound-mediated biophotonic imaging: A review of acousto-optical tomography and photo-acoustic tomography. *Dis. Markers*, 19:123–138, 2008.
- [2] DM King. Imaging of metastatic melanoma. *Journal of Hong Kong College*, 7: 66–69, 2004.
- [3] Melody J. Eide, Martin A. Weinstock, and Melissa A. Clark. Demographic and socioeconomic predictors of melanoma prognosis in the united states. *Journal of Health Care for the Poor and Underserved*, 20:227–245, 2009.
- [4] Fadi Hanbali and Raymond Sawaya. *Contemporary Cancer Research: Brain Tumors*. Humana Press Inc.
- [5] Gabriella Cohn-Cedermark, Eva Mansson-Brahme, Lars Erik Rutqvist, Olle Larsson, Toom Singnomklao, and Ulrik Ringborg. Metastatic patterns, clinical outcome, and malignant phenotype in malignant cutaneous melanoma. *Acta Oncologica*, 38:549–557, 1999.
- [6] Thompson and Shaw. Benefits of sentinel node biopsy for melanoma: A review based on interim results of the first multicenter selective lymphadenectomy trial. *Royal Australasian College of Surgeons*, 76:100–103, 2006.
- [7] Robert John Talbert. Photoacoustic discrimination of vialbe and thermally coagulated blood for burn injury imaging. Master of science, University of Missouri-Columbia, August 2007.
- [8] Baskaran Govindarajan, James E. Sligh, Bethaney J. Vincent, Meiling Li, Jeffrey A. Canter, Brian J. Nickoloff, Richard J. Rodenburg, Jan A. Smeitink, Larry Oberley, Yuping Zhang, Joyce Slingerland, Rebecca S. Arnold, J. David Lambeth, Cynthia Cohen, Lu Hilenski, Kathy Griendling, Marta Martínez-Diez, José M. Cuezva, and Jack L. Arbiser. Overexpression of akt converts radial growth melanoma to vertical growth melanoma. *Journal of Clinical Investigation*, 117(3):719–729, March 2007.

- [9] Christopher Haqq, Mehdi Nosrati, Daniel Sudilovsky, Julia Crothers, Daniel Khodabakhsh, Brian L. Pulliam, Scot Federman, James R. Miller III, Robert E. Allen, Mark I. Singer, Stanley P. L. Leong, Britt-Marie Ljung, Richard W. Sagebiel, and Mohammed Kashani-Sabet. The gene expression signatures of melanoma progression. *PNAS*, 102(17):6092–6097, April 2005.
- [10] R.S. Oliveira Filho, L.M. Ferreira, L.J. Biasi, M.M.S.S. Enokihara, G.R. Paiva, and J. Wagner. Vertical growth phase and positive sentinel node in thin melanoma. *Braz J Med Biol*, 36(3):347–350, October 2003.
- [11] Fidler I.J. Orthotopic implantation of human colon carcinomas into nude mice provides a valuable model for the biology and therapy of metastasis. *Cancer Metastasis Rev.*, 10:229–243, 1991.
- [12] E.V. Sugarbaker. Cancer metastasis: a product of tumor-host interactions. *Curr. Prob. Cancer*, 3:1–59, 1979.
- [13] Jeong hyon Kim, Jee Young Kim, Kyung Ah Chun, Won-Hee Jee, and Mi-Sook Sung. Mr imaging manifestations of skin tumors. *European Society of Radiology*, 18:2652–2661, 2008.
- [14] Anka Thies, Kersten Peldschus, Harald Ittrich, Gerhard Adam, Peter Altevogt, Christoph Wagener, and Udo Schumacher. Magnetic resonance imaging of melanoma metastases in a clinical relevant human melanoma xenograft scid mouse model. *Cancer Letters*, 274:194–200, 2009.
- [15] Estee L. Psaty, BA, and Allan C. Halpern. Current and emerging technologies in melanoma diagnosis: the state of the art. *Clinics in Dermatology*, 27:35–45, 2009.
- [16] Erich W. Stein, Konstantin Maslov, and Lihong V. Wang. Noninvasive, in vivo imaging of the mouse brain using photoacoustic microscopy. *Journal of Applied Physics*, 105, May 2009.
- [17] Hao F Zhang, Konstantin Maslov, George Stoica, and Lihong V. Wang. Functional photoacoustic microscopy for high-resolution and noninvasive in vivo imaging. *Nature Biotechnology*, 24, 2006.
- [18] Hao Zhang, Konstantin Maslov, Meng Li, George Stoica, and Lihong V. Wang. In vivo volumetric imaging of subcutaneous microvasculature by photoacoustic microscopy. *Optics Express*, pages 9317–9323, 2006.
- [19] Rinat O. Esenaliev, Alexander A. Karabutov, and Alexander A. Oraevsky. Sensitivity of laser opto-acoustic imaging in detection of small deeply embedded tumors. *IEEE*, 5(4):981–987, July/August 1999.

- [20] Alexander A. Oraevsky, Alexander A. Karabutov, Sam Solomatin, Ed Savateeva, Vic Andreev, Zed Gatalica, Hao Singh, and Rob Fleming. Laser optoacoustic imaging of breast cancer in vivo. *Proc SPIE*, pages 6–15, 2001.
- [21] Kwang Hyun Song and Lihong V. Wang. Deep reflection-mode photoacoustic imaging of biological tissue. *Journal of Biomedical Optics*, 12(6), December 2007.
- [22] Lihong V. Wang and Hsin i Wu. *Biomedical Optics - Principles and Imaging*. John Wiley & Sons, Inc., 2007.
- [23] Hao Zhang. *Functional photoacoustic microscopy*. PhD thesis, Texas A & M University, August 2006.
- [24] Jan Laufer, Clare Elwell, Dave Delpy, and Paul Beard. In vitro measurements of absolute blood oxygen saturation using pulsed near-infrared photoacoustic spectroscopy: accuracy and resolution. *Phys. Med. Biol.*, 50, 2005.
- [25] Mathangi Sivaramakrishnan. In vivo blood oxygenation level measurements using photoacoustic microscopy. Master’s thesis, Texas A & M University, May 2006.
- [26] Hao F Zhang, Konstantin Maslov, and Lihong V Wang. In vivo imaging of subcutaneous structures using functional photoacoustic microscopy. *Nature Protocols*, 2(4):797–804, April 2007.
- [27] Xueding Wang, David L. Chamberland, and Guohua Xi. Noninvasive reflection mode photoacoustic imaging through infant skull toward imaging of neonatal brains. *Journal of Neuroscience Methods*, 168:412–421, 2008.
- [28] Changhui Li and Lihong V Wang. Photoacoustic tomography and sensing in biomedicine. *Phys. Med. Biol.*, 54:R59–R90, September 2009.
- [29] Lihong V. Wang. Prospects of photoacoustic tomography. *Med Phys.*, 35(12): 5758–5767, December 2008.
- [30] Meng-Lin Li, Jung-Taek Oh, Xueyi Xie, Geng Ku, Geng Ku, Wei Wang, Chun Li, Gina Lungu, George Stoica, and Lihong V. Wang. Simultaneous molecular and hypoxia imaging of brain tumors in vivo using spectroscopic photoacoustic tomography. *IEEE*, 96, No. 3, March 2008.
- [31] Quan Zhoua, Yang Dongc, Li Huangb, Shihua Yangb, and Wenli Chen. Study of cerebrovascular reserve capacity by magnetic resonance perfusion weighted imaging and photoacoustic imaging. *Magnetic Resonance Imaging*, 27:155–162, July 2009.

- [32] L.V. Wang. Tutorial on photoacoustic microscopy and computed tomography. *IEEE*, 14, 2008.
- [33] Jung-Taek Oh, Meng-Lin Li, Hao F. Zhang, Konstantin Maslov, George Stoica, and Lihong V. Wang. Three-dimensional imaging of skin melanoma in vivo by dual-wavelength photoacoustic microscopy. *Journal of Biomedical Optics*, 11(3), 2006.
- [34] Xueding Wang. *Functional Photoacoustic Tomography of Animal Brains*. PhD thesis, Texas A & M University M University, August 2004.
- [35] Alexander Bell. On the production and reproduction of sound by light. *American Journal of Science*, pages 305–325, 1880.
- [36] Vitor Gusev and Alexander Karabutov. *Laser Optoacoustics*. American Institute of Physics, 1993.
- [37] O. Minet, K. Dörschel, and G. Müller. *Lasers in biology and medicine*, chapter 3, pages 279–303. Landolt-Börnstein.
- [38] Duck F. A. *Physical Properties of Tissue*. London: Academic.
- [39] Rachel Rinat Bitton. *A High Frequency Array-Based Photoacoustic Microscopy Imaging System*. Doctor of philosophy, University of Southern California, December 2007.
- [40] A Oraevsky, F Tittel, and S Jacques. Determination of tissue optical properties by piezoelectric detection of laser-induced stress waves. *Proc SPIE*, pages 86–101, 1993.
- [41] Minghua Xuand and Lihong V. Wangb. Photoacoustic imaging in biomedicine. *American Institue of Physics, Review of Scientific Instruments* 77, 2006.
- [42] Cope M. *The application of near infrared spectroscopy to noninvasive monitoring of cerebral oxygenation in the newborn infant*. Phd thesis, University College, London, 1991.
- [43] John A. Copland, Mohammad Eghtedari, Vsevolod L. Popov, Nicholas Kottov, Natasha Mamedova, Massoud Motamedi, and Alexander A. Oraevsky. Bioconjugated gold nanoparticles as a molecular based contrast agent: Implications for imaging of deep tumors using optoacoustic tomography. *Molecular Imaging and Biology*, 6:341–349, 2004.

- [44] Srivalleesha Mallidi, Timothy Larson, Justina Tam, Pratixa P. Joshi, Andrei Karpouk, Konstantin Sokolov, and Stanislav Emelianov. Multiwavelength photoacoustic imaging and plasmon resonance coupling of gold nanoparticles for selective detection of cancer. *American Chemical Society*, 9, No.8, May 2009.
- [45] Jan Laufer, Dave Delpy, Clare Elwell, and Paul Beard. Quantitative spatially resolved measurement of tissue chromophore concentrations using photoacoustic spectroscopy: application to the measurement of blood oxygenation and haemoglobin concentration. *Phys. Med. Biol.*, 52:141–168, 2007.
- [46] Liangzhong Xiang, Da Xing, Huaimin Gu, Diwu Yang, Sihua Yang, and Lvming Zeng. High resolution and high contrast noninvasive photoacoustic imaging of neovascularization in tumor angiogenesis. *International Conference on Complex Medical Engineering*, 2007.
- [47] Xinmai Yang, Erich W. Stein, S. Ashkenazi, and Lihong V. Wang. Nanoparticles for photoacoustic imaging. *Nanomedicine and Nanobiotechnology*, 1, issue 4, August 2009.
- [48] Konstantin Maslov, George Stoica, and Lihong V Wang. In vivo dark-field reflection-mode photoacoustic microscopy. *Opt Lett*, 30:625–627, 2005.
- [49] M. V. Yezhelyev, X. Gao, Y. Xing, A. Al Hajj, S. Nie, and R. M. O'Regan. *Lancet Oncology*, volume 7. 2006.
- [50] M. Ferrari. *Nat. Rev. Cancer*, volume 5, pages 161–171. 2005.
- [51] Pai-Chi Li, Dar-Bin Shieh, Churng-Ren Chris Wang, Chen-Wei Wei, Chao-Kang Liao, Ann-Ann Ding, Ya-Na Wu, Carolina Poe, and Suwen Jhan. In vivo photoacoustic molecular imaging with simultaneous multiple selective targeting using antibody-conjugated gold nanorods. *Nature Precedings*, March 2008.
- [52] Srivalleesha Mallidi, Timothy Larson, Jesse Aaron, Konstantin Sokolov, and Stanislav Emelianov. Molecular specific optoacoustic imaging with plasmonic nanoparticles. *Optical Society of America*, 15(11), May 2007.
- [53] Ling Tong, Qingshan Wei, Alexander Wei, and Ji-Xin Cheng. Gold nanorods as contrast agents for biological imaging: Optical properties, surface conjugation and photothermal effects. *The American Society of Photobiology*, pages 21–32, October 2009.
- [54] Xiaohua Huang, Prashant K. Jain, Ivan H. El-Sayed, and Mostafa A. El-Sayed. Plasmonic photothermal therapy (pptt) using gold nanoparticles. *Lasers Med Sci*, 23:217–228, August 2008.

- [55] N. Xu, Shu H., Marcus R. & Crocker, and I. R. Radiation necrosis after stereotactic radiosurgery for metastatic brain disease. *Int. J. Radiat. Oncol. Biol. Phys.*, 69(S163-S163), 2007.
- [56] Ahmad A Tarhini and Sanjiv S Agarwala. Management of brain metastases in patients with melanoma. *Current Opinion in Oncology*, 16(2):161–166, 2004.
- [57] Y Mori, D Kondziolka, J C Flickinger, J M Kirkwood, S Agarwala, and L D Lunsford. Stereotactic radiosurgery for cerebral metastatic melanoma: factors affecting local disease control and survival. *Int J Radiat Oncol Biol Phys*, 42(3): 581–9, Oct 1998.
- [58] et al. Roy A. Patchell. A randomized trial of surgery in the treatment of single metastases to the brain. *N. Engl. J. Med.*, 322:494–500, 1990.
- [59] Cheng Yu, Joseph C T Chen, Michael L J Apuzzo, Steven O'Day, Steven L Giannotta, Jeffrey S Weber, and Zbigniew Petrovich. Metastatic melanoma to the brain: prognostic factors after gamma knife radiosurgery. *Int J Radiat Oncol Biol Phys*, 52(5):1277–87, Apr 2002.
- [60] Xu MH and Wang LHV. Time-domain reconstruction for thermoacoustic tomography in a spherical geometry. *IEEE Trans Med Imag*, 21:814–822, 2002.
- [61] Hao F. Zhang, Konstantin Maslov, and Lihong V. Wang. Automatic algorithm for skin profile detection in photoacoustic microscopy. *Journal of Biomedical Optics*, 14(2), March 2009.